Velocity Distribution Functions of Pickup Ions with Ulysses/SWICS

MASTER THESIS

Anne Fischer
Dezember 2019

Christian-Albrechts-Universität zu Kiel
Institut für Experimentelle und Angewandte Physik
Arbeitsgruppe Extraterrestrische Physik

Abstract

Pickup ions (PUI) are former neutral atoms that are ionized in the heliosphere. The neutral atom's origin is either the interstellar medium (interstellar PUI) or a source within the heliosphere (inner-source PUI).
After ionization, the PUI's velocity distribution function (VDF) is shaped by interaction with the magnetized solar wind plasma. The general idea is that PUI are swept outwards with the solar wind and that their initially anisotropic VDF is rapidly deformed by different processes and conditions within the heliosphere. The details of involved mechanisms like e.g. pitch-angle scattering and adiabatic cooling are not completely understood to this day. A study of the evolution of the VDF helps us to understand the origin of PUI and their neutral's seed population and of the underlying effects that shape the VDF.
However, most observations of PUI are limited to 1D reduced velocity measurements in the spacecraft frame. Consequently, they do not allow for interpretations without making assumptions about the underlying VDF.
In this Master thesis I want to develop a method for resolving data measured by the Solar Wind Ion Composition Spectrometer (SWICS) onboard the spacecraft Ulysses in three dimensions. SWICS is a time-of-flight mass spectrometer that is able to determine the mass, mass-per-charge and energy of ions by independent measurements of the ion's energy-per-charge, time-of-flight and residual energy. Additionally, SWICS provides information on the inflow direction of incident ions by a three-part division of the sensor and a sectorization of Ulysses' spin. For translating this information correctly into three-dimensional velocity components it is necessary to consider Ulysses' orientation in space at any time of measurement.
In this work, I utilize a virtual detector to perform a transformation from Ulysses SWICS Pulse-Height Analysis data into three-dimensional velocity components using the example of He^+ PUI.

Zusammenfassung

Pickup-Ionen (PUI) sind ehemals neutrale Teilchen, die innerhalb der Heliosphäre ionisiert werden. Die Neutralteilchen stammen entweder aus dem interstellaren Medium (interstellare PUI) oder aus einer Quelle innerhalb der Heliosphäre (Inner-Source PUI).
Nachdem die Teilchen ionisiert wurden, wird ihre Geschwindigkeitsverteilungsfunktion (VDF) durch Wechselwirkung mit dem magnetisierten Sonnenwindplasma geformt. Die grundlegende Vorstellung ist, dass die PUI dann mit dem Sonnenwind nach außen strömen und ihre ursprünglich anisotrope VDF durch unterschiedliche Prozesse in der Heliosphäre verformt wird. Dabei sind die Details der beteiligten Mechanismen wie z.B. Pitchwinkel-Streuung oder adiabatisches Kühlen bis heute nicht vollständig verstanden. Die Untersuchung der VDF-Evolution kann sowohl dazu beitragen den Ursprung der PUI und ihrer zugrundeliegenden Neutralteilchen zu verstehen als auch die Effekte, die ihre VDF formen.
Allerdings sind die meisten PUI-Beobachtungen auf 1D-reduzierte Messungen im Bezugssystem des Spacecrafts beschränkt, weshalb sie nicht interpretiert werden können ohne Annahmen über die zugrundeliegende VDF zu machen.
In dieser Masterarbeit soll eine Methode entwickelt werden, mit der man Messdaten des Instruments SWICS (Solar Wind Ion Composition Spectrometer) an Bord des Spacecrafts Ulysses in drei Dimensionen auflösen kann. SWICS ist ein Massenflugzeitspektrometer, mit dem durch unabhängige Messungen von Energie-pro-Ladung, Flugzeit und Restenergie eines Ions dessen Masse, Masse-pro-Ladung und Energie bestimmt werden kann. Zusätzlich bietet SWICS eine Messung der Einflugrichtung von Ionen aufgrund von einer Dreiteilung des Sensors und einer Sektorisierung von Ulysses' Spin. Um diese Informationen über die Einflugrichtung korrekt in dreidimensionale Geschwindigkeitskomponenten zu überführen muss die Ausrichtung von Ulysses zu jedem Messzeitpunkt betrachtet werden.
In dieser Arbeit verwenden wir einen virtuellen Detektor, um den Übergang von Ulysses SWICS *Pulse Height Analysis*-Daten zu dreidimensionalen Geschwindigkeitskomponenten am Beispiel von He^+ PUI durchzuführen.

Contents

Chapter 1

Introduction

Understanding the physics behind interstellar PUI is of special interest as they give us a possibility to directly observe properties of the interstellar medium by in-situ measurements within the heliosphere. Additionally, the observation of their VDF helps us to understand interplanetary transport as the evolution of their characteristic VDF shows signatures of the transport processes involved. Many studies on PUI

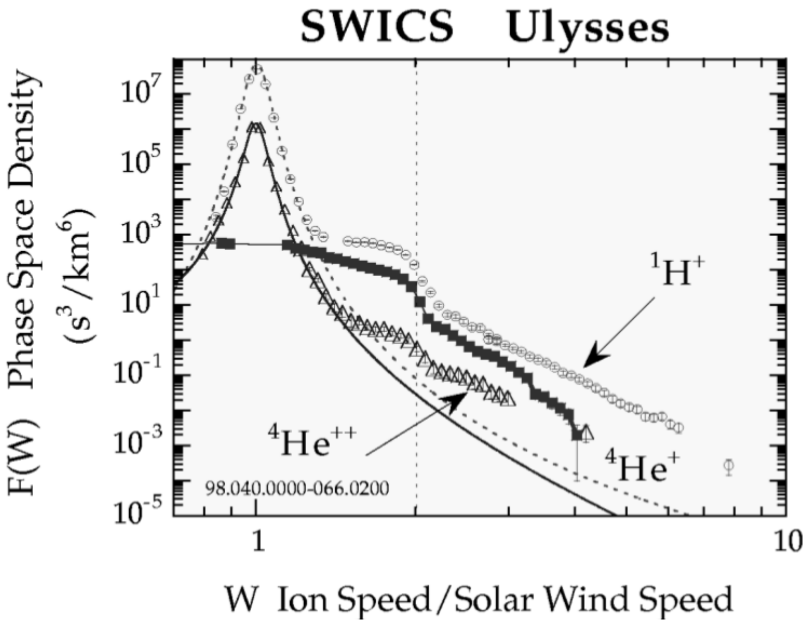

FIGURE 1.1: Phase space density for He^{2+}, He^+ and H^+ against $w = \frac{v_{ion}}{v_{sw}}$ in the slow solar wind ($v_{sw} = 375\,km\,s^{-1}$). PUI distributions are clearly visible for all three species in the w range between ~ 1.5 and 2 followed by a cutoff at $w = 2$ and high-velocity tails. Solar wind distributions are represented by the dashed and solid curves for He^{2+} and H^+. The figure is taken from Gloeckler (1999).

VDF base on measurements of Ulysses SWICS (Gloeckler et al., 1998). These studies were limited to 1D reduced observations in the spacecraft frame until today, as only the absolute values of velocities were considered. An example by Gloeckler (1999) is shown in Fig. 1.1. Here we see the phase space density of three different pickup ion species drawn against w, which is the ion's velocity divided by the current solar wind speed. The pickup ions shows a non-Maxwellian distribution with a clear cutoff at w=2. While the distributions of He2+ and H+ are superimposed by the distribution of the solar wind ions around w=1, the distribution of He+ PUI is unveiled. However, the actual PUI VDF is multi-dimensional and cannot be reproduced from the reduced 1D measurement without making assumptions on the underlying distribution. Several 3D VDF may lead to the same 1D VDF when being reduced and thus every 1D measurement is ambiguous.

As Ulysses SWICS is capable of resolving the inflow direction of incident ions, a three-dimensional VDF can be obtained when taking into account all given information. The aim of this thesis is to make use of this information and to develop a tool to provide three-dimensional VDFs. PUI differ from solar wind ions by a non-Maxwellian VDF. As this distribution is particularly broad, He+ PUI are the perfect candidates for testing the tool and for being studied with it.

The thesis starts with an introduction into PUI, before the Ulysses mission and the instrument SWICS with its measurement principle are described. In the third chapter a virtual detector is developed to translate the raw He+ data into three-dimensional velocity components. For this, SWICS' intrigue geometry has to be considered as well as Ulysses' orientation in space and its eigen-velocity. In the final section the obtained three-dimensional spectra are presented in different projections.

10

Chapter 2

Pickup Ions

A neutral atom inside the heliosphere is only subjected to the gravitational force and radiation pressure of the Sun. It is not sensitive to any electromagnetic forces until it becomes ionized by solar ultra-violet radiation, charge exchange with solar wind protons or electron impact (Rucinski et al., 1996). After ionization the particle starts interacting with the solar wind plasma. In particular it is forced onto a gyro orbit about the heliospheric magnetic field that is embedded within the solar wind. As the freshly created ion is swept away with the magnetic field line it is "picked up" from its location of ionization – a new pickup ion (PUI) has been created.

PUI are mostly only singly charged. This characteristic can help to distinguish them from solar wind ions of coronal origin which often have been ionized multiple times, if not completely. Additionally, PUI are characterized by a broad, non-Maxwellian Velocity Distribution Function. This is formed by the pickup process and the following interaction with the magnetized solar wind plasma, which will be described in more detail in Sec. 2.3.
PUI were observed for the first time by Möbius et al. (1985) as He^{+} with the SULEICA Instrument on the AMPTE spacecraft at 1 AU. Since then, a variety of other PUI species like H^{+}, He^{2+} or C^{+}, N^{+}, O^{+}, Mg^{+}, Si^{+} and Fe^{+} has been observed.
There are two possible origins for the PUI's neutral seed population. One of them is the interstellar medium, the other a source inside the heliosphere.

2.1 Interstellar Pickup Ions

The heliosphere can be imagined as a big bubble that is blown up by the solar wind and confined by the heliopause. This bubble is embedded in the Local Interstellar Medium (LISM), which moves with a velocity of $\sim 25\,\mathrm{km\,s^{-1}}$ relative to the heliosphere. As the LISM is a relatively cold plasma with $T_{LISM} \sim 7000\,\mathrm{K}$ (Frisch et al., 2011), it is not completely ionized. The neutral part of the LISM can enter the heliosphere as it is not deflected by the heliosheath. Due to the relative motion of the LISM against the heliosphere, a continuous stream of neutral particles enters the heliosphere.
Inside the heliosphere the neutrals are guided only by the gravitational force and radiation pressure of the Sun. The neutral particle's species determines how deep it can travel into the heliosphere before it becomes ionized. Species with a higher First Ionization Potential will be able to approach the Sun much further without being ionized (Kallenbach et al., 2000). This results in He^{+} being the dominant PUI species at a solar distance of 1 AU even if in the LISM the abundance of H is about ten times the one of He (Frisch et al., 2011).

2.2 Inner-source Pickup Ions

The idea of an additional source for the PUI's neutral seed population was born when Geiss, Gloeckler, Fisk, et al. (1995) measured a global distribution of C^+ PUI with the SWICS instrument on Ulysses. Interstellar C exists almost exclusively in a singly charged state (**Frisch**) in the LISM. As only neutral atoms can enter the heliosphere it was not expected to find a significant signature of C^+ PUI. However, PUI C^+ was observed with about the same ratio as O^+ PUI, of which, in contrast, 80% is in a neutral charge state in the interstellar medium. These findings suggested that there must be another source for neutrals that has its origin somewhere inside the heliosphere. In following studies (e.g. Geiss, Gloeckler, and Steiger, 1995) there were found also other species like O^+ and Ne^+ of these, so called, inner-source PUI.
Inner-source PUI show a composition that is similar to the one of the solar wind (Gloeckler et al., 2000; Allegrini et al., 2005) as well as a VDF that is centered around $w_{sc} \approx 1$ (Schwadron et al., 2000) and seems to have thermalized with the solar wind. However, inner-source PUI are not completely understood until today. In particular the production mechanism of their neutral seed population is under debate. Allegrini et al. (2005) have summarized current candidates for possible scenarios. Two of those give an explanation for the ions' composition as they directly incorporate solar wind ions in the process:

- Solar wind recycling (Gloeckler et al., 2000; Schwadron et al., 2000): Absorption of solar wind ions by heliospheric grains and subsequent reemission of neutral atoms

- Solar wind neutralization (Wimmer-Schweingruber et al., 2002): Solar wind ions penetrate sub-micron-sized dust grains and undergo (partial) neutralization by charge exchange

However, as this work does not focus on inner-source PUI in particular and as we do not know their production mechanism for certain, the following considerations mainly relate to interstellar PUI.

2.3 Pickup Ion Velocity Distribution Function

For understanding the initial shape of the PUI VDF one needs to consider the pickup process itself.
For neutrals from the LISM their initial speed v_{ini} before being ionized is mainly given by the inflow speed v_{LISM} of the local interstellar medium with which they enter the heliosphere. Schwadron et al. (2015) obtained $v_{LISM} \approx 25\,\mathrm{km\,s^{-1}}$ for He with the IBEX satellite. Considering the acceleration by the Sun's gravitational force we have a maximum initial speed of $v_{ini} \approx 50\,\mathrm{km\,s^{-1}}$ at 1 AU. Compared to an average solar wind speed of $v_{sw} \approx 400\,\mathrm{km\,s^{-1}}$ one can neglect this initial speed in a first step. For simplicity we thus consider a neutral particle at rest that becomes ionized by one of the aforementioned processes. The freshly created ion is now subjected to the electromagnetic forces of the solar wind plasma. In particular, it finds itself at a velocity v_{sw} relative to the magnetic field which is convected outwards by the solar wind that is assumed to flow radially outwards. Due to the Lorentz force the PUI starts to gyrate about the magnetic field line on an orbit that is perpendicular to the field line. When we further consider a magnetic field's orientation that is perpendicular to the solar wind flow, $\vec{B} \perp \vec{v}_{sw}$, the ion's gyration speed is v_{sw} while its guiding center moves together with the field line at a speed of v_{sw} as well. Thus, the total

speed of the PUI ranges between $0\,\mathrm{v_{sw}}$ and $2\,\mathrm{v_{sw}}$ in a Sun frame of reference, s. Fig. 2.1. As the heliospheric magnetic field lines are shaped like an Archimedean spiral,

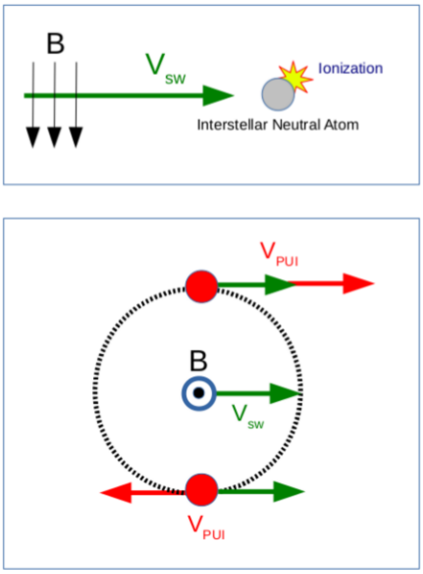

FIGURE 2.1: Visualization of the pickup process. We assume a neutral particle at rest and a magnetic field moving perpendicular to the solar wind and at solar wind speed relative to the particle (upper panel). Being ionized in this situation, the particle is forced onto a gyro-orbit about the magnetic field line. The ion's total velocity then ranges from $0\,\mathrm{v_{sw}}$ to $2\,\mathrm{v_{sw}}$ in a Sun frame of reference (lower panel). The figure is taken from Taut et al. (2017).

the so-called "Parker Spiral", the assumption of a perpendicular magnetic field only applies when solar wind speed v_{sw} and solar distance $r_\odot$ follow the relation

$$90^\circ \approx \arctan\left(\frac{2\pi}{T_\odot \cdot v_{\mathrm{sw}}} r_\odot\right)$$

with the Sun's sidereal period $T_\odot \approx 25\,\mathrm{d}$ (Prölss, 2004). In other cases, e.g. for solar distances about 1 AU, at which the angle between solar wind and magnetic field direction is approximately 45°, the maximum speed in a Sun frame of reference is decreased.

The velocity space for a pickup situation with a non-radial magnetic field orientation is shown in a 2D projection in Fig. todo. Here the PUI's total velocity consists of the movement of the guiding center (...todo) and the gyration velocity (...todo). We note that in this case there is a relative velocity between the motion of the solar wind bulk and the PUI's guiding center movement. However, independent of the magnetic field orientation, every possible velocity space trajectory is part of a spherical shell with the radius v_{sw} centered around $\vec{v}_{\mathrm{sw}}$. That means that, in the frame of the solar wind, the freshly created PUI always moves with a speed that is as fast as the solar wind itself.

Instead of a single PUI we can consider an ensemble of PUI that is injected into the solar wind while the magnetic field orientation is not changing significantly. In this scenario we expect the VDF to form a ring shape in velocity space, commonly called the "PUI torus VDF" (Oka et al., 2002). The expected orientation of this highly anisotropic VDF depends on the local magnetic field direction and is sketched in

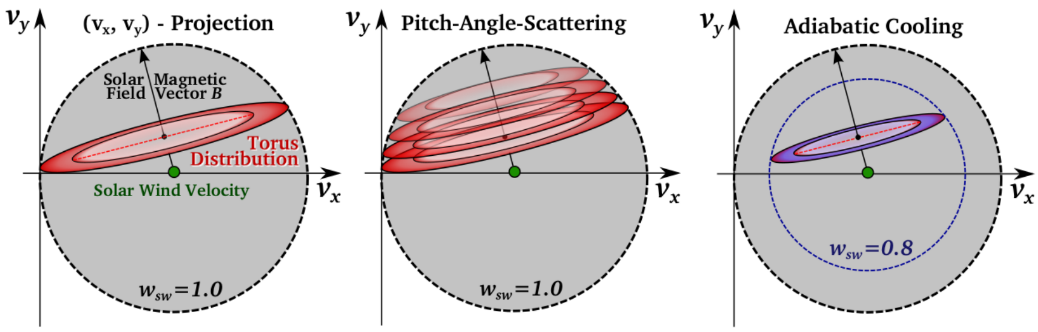

FIGURE 2.2: Velocity space diagrams for an initial PUI torus distribution (left), the same distribution under the influence of pitch-angle scattering (center) and after the distribution has been "cooled" (right). For a better visibility of the torus character the $v_x - v_y$ plane is slightly tilted. The figure is from Drews et al. (2015), modified.

Fig. 2.2, left panel, for a magnetic field direction that is slightly tilted from a perpendicular direction relative to the solar wind. After the injection, the PUI population is radially carried away with the solar wind. During phase space transport through the heliosphere the PUI are subjected to multiple processes that are expected to modify the shape of the initial toroidal VDF. However, it is not completely understood how the VDF evolves in detail.

A fast isotropization of the VDF due to pitch-angle scattering was suggested by Vasyliunas et al. (1976) in a theoretical work. This would result in a VDF that is distributed across the complete surface of the spherical shell with radius v_{sw}. Fig. 2.2, center, shows the initial influence of pitch-angle scattering.

However, observations by e.g. Möbius et al. (1998) on He^+ or Gloeckler et al. (1995) on H^+ have shown clear anisotropic features in the measured VDF. Following studies (e.g. Isenberg, 1997) tried to explain these findings with the assumption that the ions would be injected more likely into the sunward hemisphere of velocity space. Ineffective pitch-angle scattering into the antisunward hemisphere would thus result in a radial anisotropy.

Recent observations have emphasized the influence of the magnetic field direction on the measured anisotropy. Utilizing 2D analyses of the velocity space, Oka et al. (2002) and Drews et al. (2015) found that the measured VDF of PUI is systematically oriented around the direction that is perpendicular to the magnetic field. Thus, it is believed that the VDF's anisotropic features are remnants of the initial toroidal VDF as the pitch-angle scattering is not as effective as assumed originally.

Furthermore, there are different acceleration and deceleration processes that change the PUI's initial VDF and lead to a diffusion in velocity space. The general idea of a toroidal distribution that has undergone some deceleration is shown in Fig. 2.2, right.

Under the assumption of an isotropic VDF the PUI population is often treated as an adiabatic gas that is consequently "cooled" when expanding with the solar wind (Vasyliunas et al., 1976). Another cooling mechanism, called the *magnetic cooling*, is due to the magnetic field weakening with solar distance. When the PUI are swept outwards both their magnetic moment and their "Complex Ginzburg-Landau invariant" (Fahr, 2007) have to be conserved. This leads to a decrease in both velocity components (parallel and perpendicular to the magnetic field) and thus to a decrease in total velocity in the frame of the solar wind. For a more detailed description of these effects see e.g. Fahr et al. (2011).

However, all of these theories assume an isotropic PUI VDF and thus must be reviewed carefully.
Acceleration of PUI can be caused by several processes. Among those are interplanetary shock waves resulting from Coronal Mass Ejections or Stream Interaction Regions, that are generally known as drivers for particle acceleration in the heliosphere (Kallenrode, 1998, Ch. 7.5). Additional possible mechanisms, including the "pump acceleration", are described in Fisk et al. (2012). Just as the aforementioned cooling processes the acceleration of PUI is still not completely understood.

Chapter 3

Instrumentation

3.1 Ulysses

The Ulysses spacecraft (Wenzel et al., 1992) was launched in 1990 and orbited the Sun for nearly 20 years as a joint ESA/NASA project. Ulysses' most remarkable feature is its out-of-ecliptic orbit with a maximum heliographic latitude of 80.1 °. It was hence the first spacecraft that was capable of taking in situ measurements from above the poles of the Sun.
The primary goal of the mission was to study the heliosphere in three dimensions. Some of the original main objectives were:

- to study the interplanetary magnetic field and the solar wind, especially its composition, the origin and waves and shocks within the solar wind plasma
- to investigate galactic cosmic rays and energetic particles
- to improve the knowledge about interplanetary dust
- to explore the neutral component of interstellar gas

Some secondary objectives included e.g. the investigation of Jupiter's magnetosphere during the Jupiter flyby and the search for gravitational waves and for gamma-ray burst sources (Wenzel et al., 1992).
To achieve these aims Ulysses was equipped with a wide range of different instruments and antennas. One of the in situ instruments is the Solar Wind Ion Composition Spectrometer (SWICS), that will be described in the next section.
A sketch of Ulysses' unique orbit is shown in Fig. 3.1. Ulysses was launched in October 1990 and left Earth's gravitational field with 15.4 km/s. Starting with a flyby maneuver around Jupiter Ulysses was sent onto its highly elliptical orbit. With an orbital period of 6.2 years Ulysses completed nearly three orbits around the sun until terminated in June 2009 due to the expiring of the radioisotope thermal generators. Within the mission's long lifetime the Sun's behavior over its activity cycle of 22 years could be studied.
Ulysses is a spin-stabilized spacecraft that spins at 5 rpm. The spin axis is aligned with the high-gain antenna's electrical axis, that provided a communication link from the spacecraft to Earth. The downlink bitrate was variable with up to 1024 bit/s during real-time connection.

3.2 SWICS

The Solar Wind Ion Composition Spectrometer (SWICS, Gloeckler et al. (1992)) is a time-of-flight mass spectrometer mounted on the spacecraft Ulysses (s. Sec. 3.1).

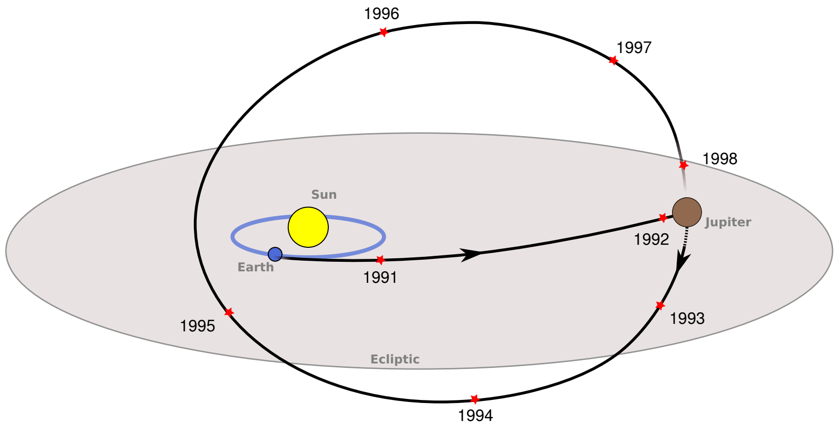

FIGURE 3.1: A sketch of Ulysses' first orbit. After the launch from Earth in 1990 the spacecraft was sent to Jupiter from where it left the ecliptic on an elliptical orbit around the sun with perihelion at 1.3 AU and aphelion at 5.4 AU. Due to the orbit's high latitude of $\sim 80^\circ$ Ulysses crossed the Sun's pole regions two times between 1994 and 1996. Figure after European Space Agency (2019).

The instrument is designed to determine the elemental and charge-state composition and the velocity distribution of solar wind ions. With an energy-per-charge range from 0.16 keV/e to 59.6 keV/e SWICS is able to measure every solar wind ion species from protons to iron with any typical charge state. Depending on the individual ion, particle energies from 1 keV up to 1 MeV are covered.
SWICS is mounted on the sun-facing side of Ulysses and revolves around the spacecraft's spin axis with the spacecraft spinning. A photograph of the instrument is shown in Fig. 3.2, left.
Ulysses SWICS also has a twin instrument that is the SWICS spare model, which has been mounted on the ACE spacecraft (Stone et al., 1998). SWICS measures the mass m, the charge q and the energy E of entering ions by a combination of three separate measurements: The electrostatic deflection analyzer within the entrance systems is used for determining the energy-per-charge of a particle. Within the time-of-flight/energy section the particle's time-of-flight and residual energy are measured. A more detailed description of the measurement is given in the next sections. A particle's trajectory through the instrument is sketched in the schematic in Fig. 3.3.

3.2.1 Collimator and Electrostatic Analyzer

Particles enter the instrument through the entrance collimator. It restricts particles to the ones with a trajectory that is parallel to the collimator slits. The collimator features an intricate geometry that is fan-shaped with an opening angle of 69° in width and 4° in height and that is at the same time curved along its width. Fig. 3.2, left panel, gives an idea of the shape.
After having entered through the collimator a particle has to pass the electrostatic analyzer. It is split up into two sections – energies-per-charge from 0.16 to 14 keV/e are covered by the proton/helium channel. Particles within this range of energy will be filtered by their energy-per-charge and after a post-acceleration will be counted by a solid-state detector. As this simple measurement principle is very limiting for our analysis we will focus on the main channel that is suitable for a full *mass/mass-per-charge* analysis.

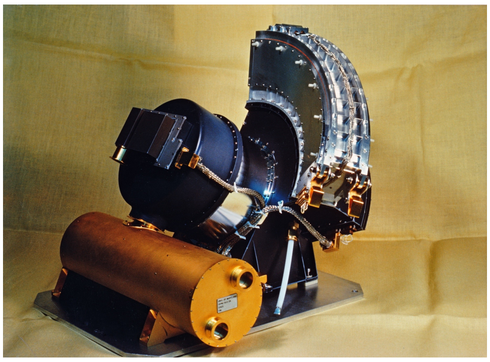

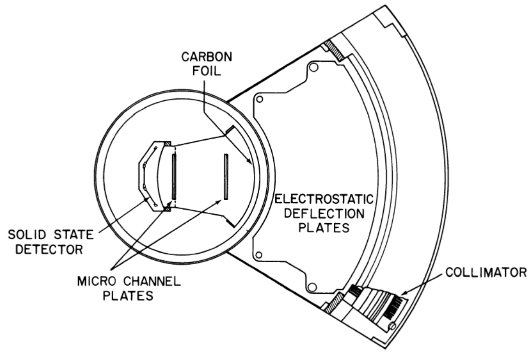

FIGURE 3.2:
Left: Photograph of the SWICS instrument. The fan-shaped collimator on top of the electrostatic deflection analyzer can bee seen on the right. It is followed by the cylindrically shaped and silvery colored *high-voltage bubble*, that contains the time-of-flight system, analog electronics and the sensor power supply. The gold-plated cylinder houses a −30 kV voltage supply. The opening angles of the collimator are 69° in width and 4° in height.
Right: Schematic cut through the sensor. In this view the orientation of the three solid state detectors is visualized.
Both figures are from from Gloeckler et al. (1992).

The main channel covers an energy-per-charge range of 0.66 to 60.51 keV/e. A particle can only pass through the pair of curved deflection plates if its kinetic energy-per-charge equals a certain ratio that is given by the voltage between the two plates. To measure particles of different energy-per-charge the deflection voltage is stepped through 64 logarithmically spaced values, s. Fig 3.4. As the voltage steps once per spin of Ulysses (every 12 s), a complete voltage cycle lasts $\sim$ 12.8 minutes. Every step has a relative uncertainty in energy-per-charge of $\Delta \mathrm{EpQ}/\mathrm{EpQ} = 5\%$ (Gloeckler et al., 1992).

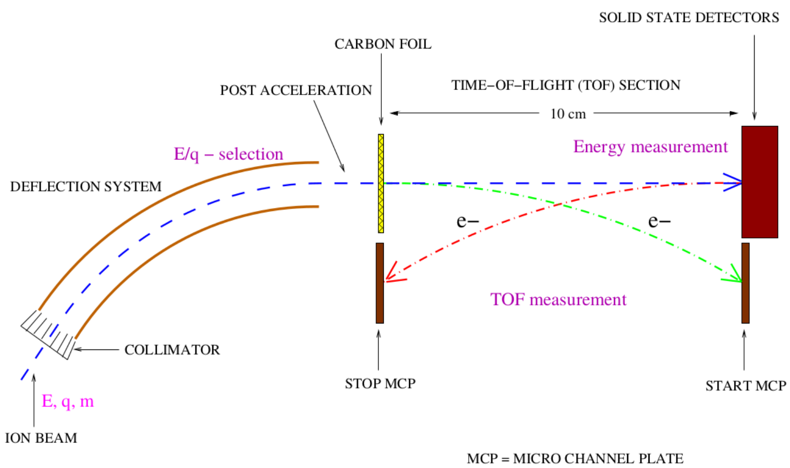

FIGURE 3.3: Schematic view of the SWICS detector. See text for reference. This figure is taken from Berger (2008).

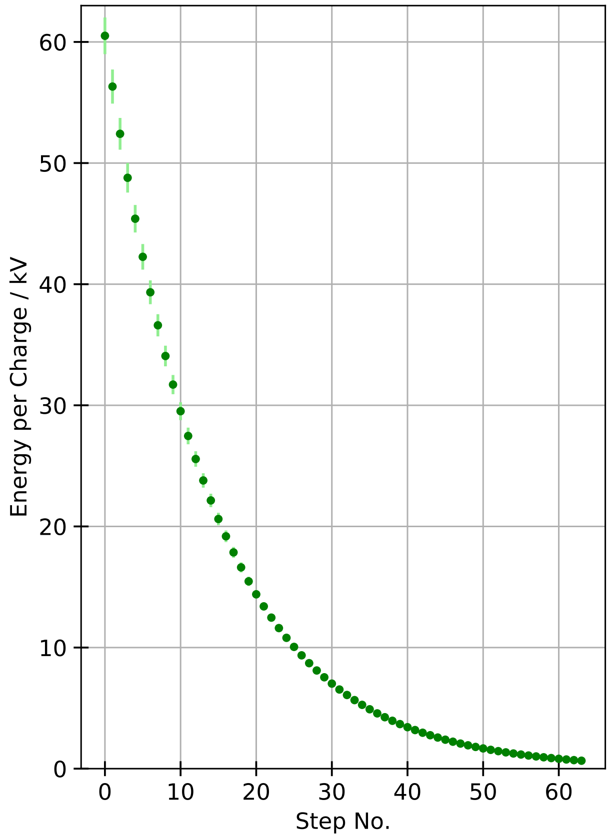

FIGURE 3.4: Energy-per-Charge steps of Ulysses SWICS. A voltage cycle starts with step 0 that is the highest voltage $EpQ = 60.51\,\mathrm{keV/e}$. Voltage is then swept down to $EpQ = 0.66\,\mathrm{keV/e}$ using 64 logarithmically spaced steps. The uncertainty of the single steps is $\frac{\Delta EpQ}{EpQ} = 5\%$ and drawn in lighter color.

3.2.2 Time-of-flight measurement

After having passed the electrostatic analyzer the ion is post-accelerated by a constant potential drop of $\sim 23\,\mathrm{kV}$. It enters the time-of-flight chamber penetrating a thin ($\sim 3\,\mu\mathrm{g/cm^2}$) carbon foil from which secondary electrons are emitted. These electrons are guided to a microchannel plate detector where a start signal is triggered (s. Fig 3.3). The stop signal is triggered after the ion has traversed nearly force free a distance of 10 cm through the vacuumized time-of-flight section. Here it hits one of the solid-state detectors, where secondary electrons are emitted again. By combining the times of the start and the stop signal the particle's time-of-flight has been measured.

3.2.3 Energy measurement

Additionally, the ion's energy is measured when it hits one of the three solid state detectors.
A solid-state detector is realized by applying an inverse bias voltage to a semiconductor material. When ionized particles hit the material, they set free charge carriers from the resulting depletion zone. These charge carriers can be measured as a pulse of current which is proportional to the deposited energy of the ion.

Each of the three detectors has an active area of 1.5x1.3 cm^2. Their alignment with each other can be seen in Fig. 3.2, right panel: While the central detector is oriented perpendicular to the symmetry axis of SWICS, the other two detectors are slightly tilted with respect to this axis. This way particles with different angles of incidence along the width of the collimator can be detected. The information of which of the three detectors has been hit will be utilized in Chapter 4 for a coarse directional resolution of incident particles.

One of SWICS' main objectives is the measurement of the composition of incident particles. An ion and its charge state can be fully identified with the knowledge of its mass m and its mass-per-charge mpq. With the measurement of the time-of-flight Tof, the energy E_{SSD} and the knowledge of the energy-per-charge EpQ we can calculate the mass m, the mass-per-charge mpq and velocity v of an ion i with the following set of equations:

$$m_i = 2\,E_{SSD}\left(\frac{Tof}{d}\right)^2 \tag{3.1}$$

$$mpq_i = 2\,(EpQ + V_{PAC})\cdot\left(\frac{Tof}{d}\right)^2 \tag{3.2}$$

$$v_i = \sqrt{2\,EpQ\,\frac{1}{mpq_i}}, \tag{3.3}$$

where d is the length of the time-of-flight section and V_{PAC} is the post-acceleration voltage. v denotes the ion's initial velocity when entering the instrument and is not to be confused with its velocity during the time-of-flight measurement, that is altered particularly by the post-acceleration.

3.3 Pulse-Height Analysis Data

Direct Pulse-Height Analysis data (PHA data) are one of SWICS' data products and the ones that are most relevant for the analysis in this work.
Over one voltage cycle SWICS steps through the 64 energy-per-charge steps of the electrostatic analyzer (s. Sec. 3.2.1), which we call ESA steps. At normal spacecraft telemetry rates SWICS steps once per spin, which is once every 12 s. From the total number of PHA words that is measured only 30 words can be transmitted per spin period. The selection is based on a priority scheme that is described below in Sec. 3.3.2.
Every 24-bit PHA word contains the following information on an incident particle that triggered a valid measurement:

- E_{SSD}: Energy deposition in the solid state detector
  measured through 256 channels in a range $40 - 600$ keV
- *ToF*: Time-of-Flight
  measured through 1024 channels in a range $10 - 200$ ns
- Sector information:
  SWICS divides one spin of Ulysses into 8 sectors of approximately equal duration. This results in information of the spatial origin of particles.
- Detector information:
  Which of the three solid state detector elements has been triggered?

- Priority category:
  Due to limited telemetry only an assorted sample of all measured particles can be transmitted. This selection is based on different priorities. For details s. Sec. 3.3.2.

The interpretation of a set of PHA words that have been collected over time is discussed in Sec. 3.4.

3.3.1 Detection Efficiency

When working with SWICS – like for any physical measurement – one has to consider several constraints that impede the ideal measurement as it is described in Sec. 3.2.
One of these constraints is the detector ion efficiency, which describes the probability to measure a particle that has entered the instrument. With an ion passing through the time-of-flight section there is the likelihood that secondary electrons may not be emitted properly from the carbon foil and the solid-state detector which then leads to an invalid time-of-flight measurement. Also, ions could pass through the time-of-flight section on divergent trajectories due to scattering processes, e.g. in the carbon foil. Subsequently, the ion possibly does not hit the sensitive area of the solid-state detector and would neither trigger a stop signal for the time-of-flight measurement nor a valid energy measurement.
Another reason for an invalid energy measurement in the solid-state detector can be that the ion's energy is smaller than the threshold of the solid-state detector. In this case, only energy-per-charge and time-of-flight information for the ion are available. Such events without a corresponding energy measurement are called double coincidences, while events with triggered start and stop signal and an energy measurement are called triple coincidences.
The reason for choosing a non-zero threshold is to limit the influence of the solid-state detector's natural noise. For SWICS this noise level is quite high, at around 12 keV (Gloeckler et al., 1992), so that the threshold is chosen to be $\sim$ 30 keV. The detection efficiency is highly dependent on the ion species and the deflection step. Ions with a small mass and charge are most likely to not overcome the threshold at low energy-per-charge values. For the bulk of He^+ this is already the case for ESA step 17 ($EpQ = 17.86\,\mathrm{keV/e}$), which corresponds to a He^+ velocity of $v = 900\,\mathrm{km\,s^{-1}}$ (s. Eq. 3.3).
Unfortunately, He^+ detection efficiencies are not known to us for Ulysses SWICS. Instead, we make use of the efficiencies from ACE SWICS, that have been calculated by Köten (2009). ACE SWICS has a different type of solid-state detector with a lower threshold than Ulysses SWICS. Thus, the detection efficiencies are different as well. As ACE SWICS also features different energy-per-charge ranges the values for Ulysses SWICS had to be extrapolated. For the highest energy-per-charge value $EpQ = 60.51\,\mathrm{keV}$ I interpolated the efficiency from the ACE He^+ triple efficiencies and then extrapolated linearly to an efficiency of 0 at ESA step 17. By this means, we accommodate for the above mentioned fact that He^+ does not have enough energy to deposit energy above the solid state detector's threshold at ESA step 17 and thus, the probability for a triple coincidence is zero. He^+ efficiencies from ACE SWICS and the resulting efficiencies used for Ulysses SWICS are shown in Fig. 3.5. For sure, these values are not realistic but represent the overall trend of a decreasing efficiency for higher ESA steps.

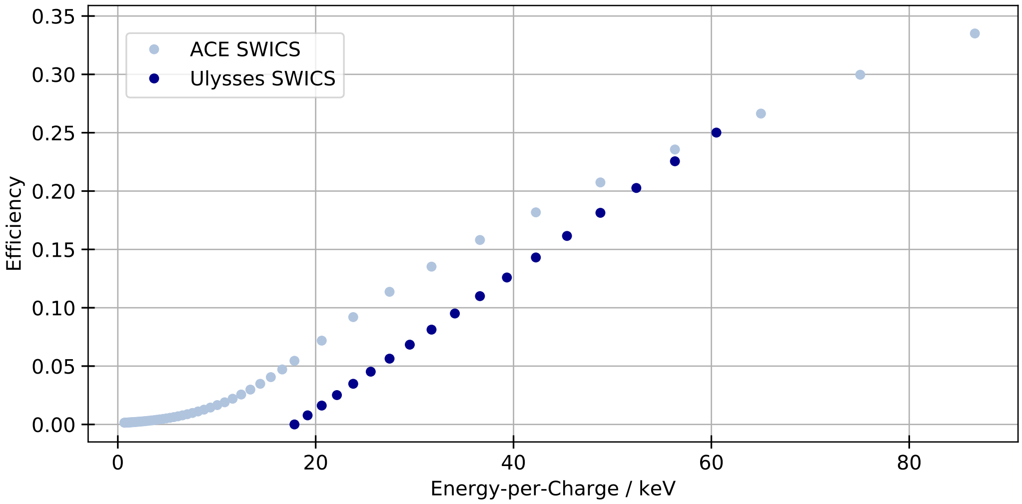

FIGURE 3.5: He^{+} detection efficiencies for ACE SWICS over all ESA steps from 0.66 keV/e to 86.64 keV/e. For Ulysses SWICS the efficiencies have been extrapolated between 0 for ESA step 17 (EpQ = 17.86 keV/e) and the highest efficiency for ESA step 0 (EpQ = 60.51 keV/e). The latter value has been interpolated from the ACE efficiencies.

3.3.2 Priority Weighting

SWICS' data processing unit performs an on-board mass and mass-per-charge-classification. For every ion with valid measurements the mass m and mass-per-charge mpq are calculated based on the measurements of E_{SSD}, ToF and the particle's ESA step using a look-up-table technique.

On the one hand these values are used for sorting the ions into predefined boxes in the m-mpq-space which yield in the so-called matrix rate, a second data product that is provided beside the PHA words.

Secondly, and more important for our analysis, the m and mpq information is used to sort every measured ion into one of three priority ranges. Due to a limited telemetry possibly not every measured particle can be transmitted as a PHA word. 30 PHA words per spin are chosen from these ranges in a way that the ratio of low and high priority PHA words is balanced. By this selection less abundant heavier ions are artificially enhanced which is necessary to recreate the measured composition from the transmitted PHA words. Table 3.1 shows a summary of this priority scheme. Details about this can be found in Gloeckler et al. (1992).

To account for the priority biased selection of PHA words it is necessary to weight the transmitted data with the so-called base-rate weight $brw = \frac{D_{\mathrm{PHA}}}{T_{\mathrm{PHA}}}$, where T_{PHA} is the number of transmitted PHA words from a m-mpq-box and D_{PHA} the number of detected particles which have been measured and been assigned to this m-mpq-box. The measured composition can be restored in this way.

TABLE 3.1: SWICS' priority categorization scheme

Range 0	$m < 8.7\,\mathrm{u}$	H, He^{+}, He^{2+}
	$m_0 : mpq < 3.3\,\mathrm{u}$	Doubles
Range 1	$m > 8.7\,\mathrm{u}$	Heavier ions
Range 2	$m_0 : mpq > 3.3\,\mathrm{u}$	Doubles

3.4 ET-Matrices

Fig. 3.6 shows longterm PHA data collected over two years with Ulysses SWICS for ESA step 24 ($EpQ = 10.8\,\mathrm{keV/e}$). Histogrammed are E_{SSD} channels and time-of-flight channels for particles with valid time-of-flight and energy measurements. As a particle's mass and mass-per-charge are connected to the measured values EpQ, ToF and E_{SSD} by Eq. 3.1 – 3.3, every ion species occupies a distinct position in this histogram, which we call ET-matrix. However, due to uncertainties in the measurements of EpQ, ToF and E_{SSD} an event may be displaced around its ideal position. For multiple events of the same species this results in broadened distributions. A detailed discussion on these uncertainties can be found for example in Berger (2008). We can identify several ion species in the shown ET-matrix: A selection of those is labeled in Fig. 3.6.

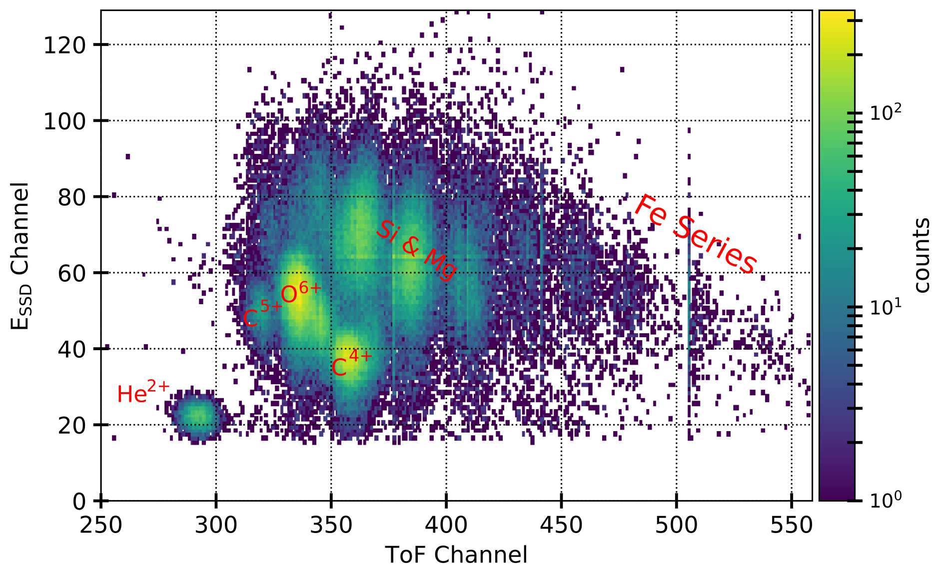

FIGURE 3.6: ET-matrix from Ulysses SWICS PHA data of years 1993-1994. All plotted events were measured during ESA step 24 ($EpQ = 10.8\,\mathrm{keV/e}$). Only triple coincidences are shown. Besides accumulated counts in ion-specific positions, there are a few horizontal and vertical stripes apparent in the shown ET-matrix – for example in E_{SSD} channel 65 and time-of-flight channel 377, 409 or 505. These are imprints of irregularities within SWICS' Analog-Digital-Converters which can be noticed as a saturation of one bin while the adjacent bin is depleted. However, these signatures are not expected to have a significant effect on the following analysis.

3.4.1 Selection of He^+

For extracting only the He^+ events from the PHA data we histogram the events' energy-per-charge against their measured time-of-flight in Fig. 3.7. Ions with the same mass-per-charge can be tracked on curves with ESA $\sim ToF^2$, while species with higher masses-per-charge can be found on curves at higher ToF channels. This way one can identify for example H^+ and He^{2+}.

At the bottom of Fig. 3.7 suprathermal He^+ clearly stands out. For time-of-flight channels above $\sim$ 375 heavier solar wind ions with similar mass-per-charge ratios

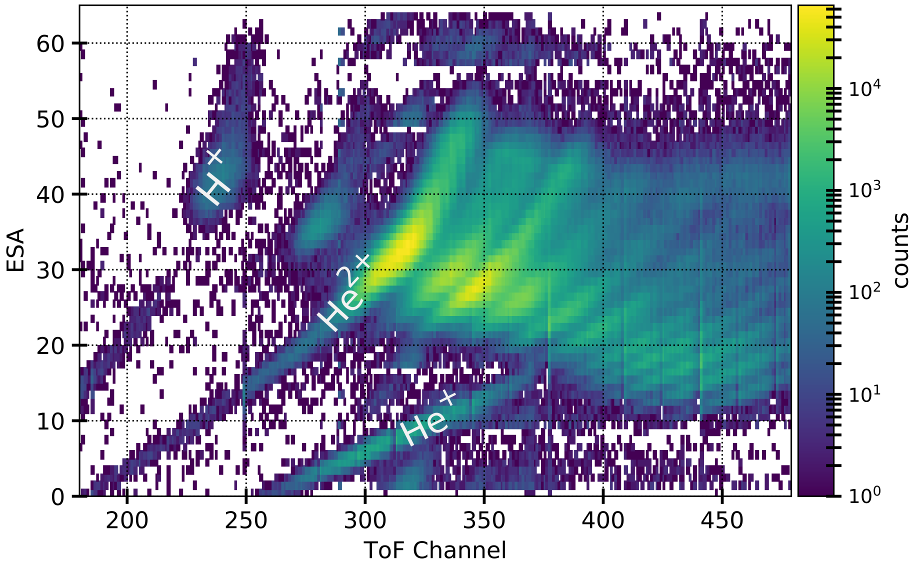

FIGURE 3.7: Histogram of time-of-flight and ESA steps of two years (1993-1994) of Ulysses SWICS Triple Coincidence PHA data. Note, that the ESA channel numbers are inversely proportional to the energy-per-charge values. Ion species with the same mass-per-charge ratio can be detected on curves $ESA \sim ToF^2$.

(e.g. Si^{7+}) mix into the He^+ population. We can take advantage of SWICS' on-board priority weighting, that has been described in Sec. 3.3.2. If we use Triple Coincidences with priority Range-0 only, events with $m < 8.7\,u$ are selected. This leaves us mainly with H^+, He^{2+} and He^+ as the prominent ions in the Range-0 mass range. The result is shown in Fig. 3.8. One can also see traces of heavier ions seeping into the Range-0 regime but this does not affect those ESA steps in which He^+ is present. For a final selection we define a box around the He^+ population and extract all events within this box. The result is shown in the upper panel of Fig. 3.9.
As explained in Sec. 3.3.1, with respect to He^+ we are limited to ESA steps 0 to 19 when only considering Triple Coincidences. For higher ESA steps He^+ only occurs as a double coincidence. Double coincidences are not sufficient for us, as we need to know which solid-state detector has been triggered for a directional analysis.
The presented selection procedure has been performed on the complete data set from 1991 to 2009 resulting in a total of $\sim 1.6 \cdot 10^5$ He^+ PHA words and an average of $\sim 8.5 \cdot 10^3$ He^+ PHA events per year. This corresponds in average to one measured He^+ event every five voltage cycles. Note, that there is a wide variation between different periods of time. PHA numbers per year are shown in Fig. 4.11.

3.4.2 Selection of He^{2+}

For testing the virtual detector in Sec. 4.2.3 we need a species of which we know that it mainly moves with the solar wind bulk and that occurs within the Triple Coincidences, so that we have directional information. We choose for He^{2+}, the most abundant ion in the solar wind (Prölss, 2004, ch. 6.1) as it also occurs in Range 0 and is easily recognizable in Fig. 3.8. Unlike He^+, He^{2+} can also be found at ESA steps higher than step 19, as it gains more energy when being post-accelerated due to the twice as high charge. Thus, He^{2+} is more likely to deposit energies above

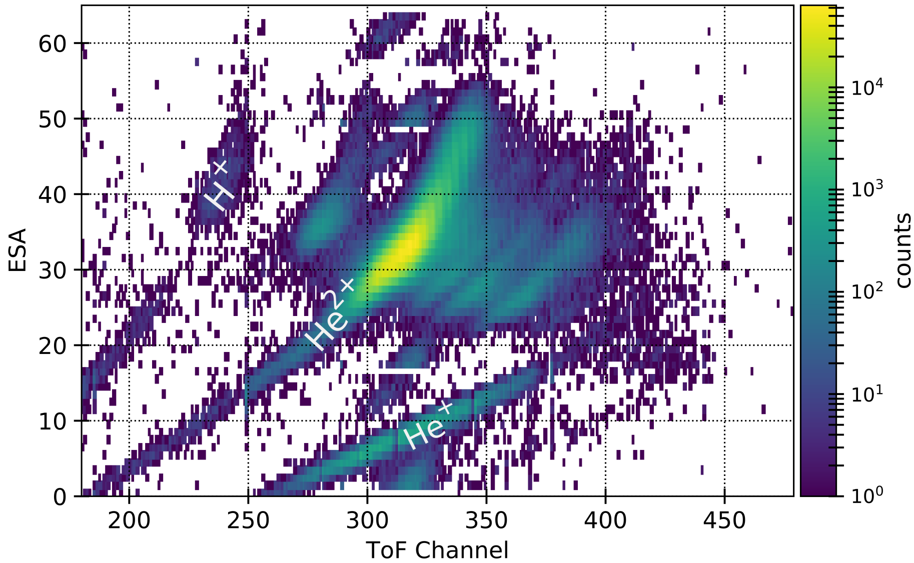

FIGURE 3.8: The same histogram as in Fig. 3.7, but this time only events with Range-0 priority are plotted. This basically removes ions with $m > 8.7\,\mathrm{u}$.

the threshold of the solid-state detector. We select He^{2+} with the same procedure as He^{+}. However, in this case it is not so crucial to include exactly every He^{2+} event, as we do not want to perform a full analysis with He^{2+}. The resulting selection is shown in Fig. 3.9, lower panel.

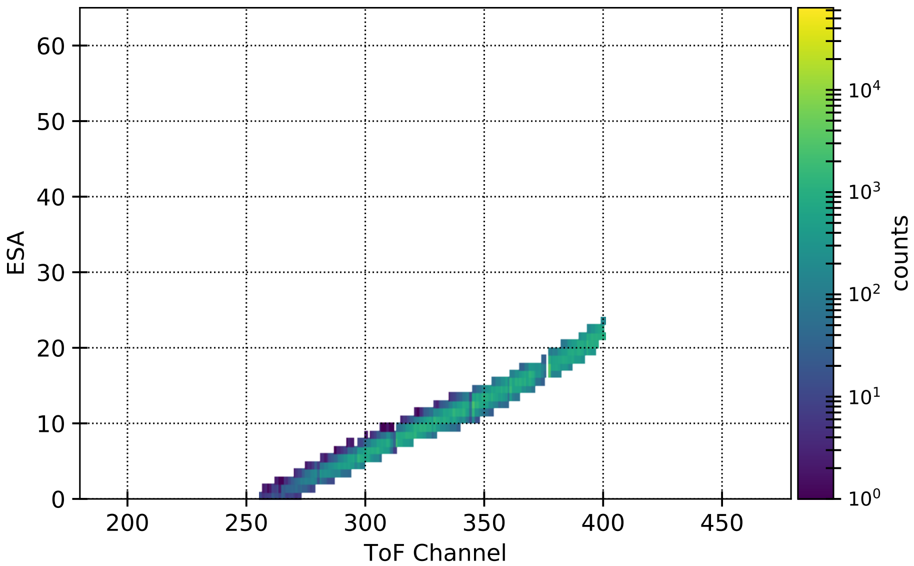

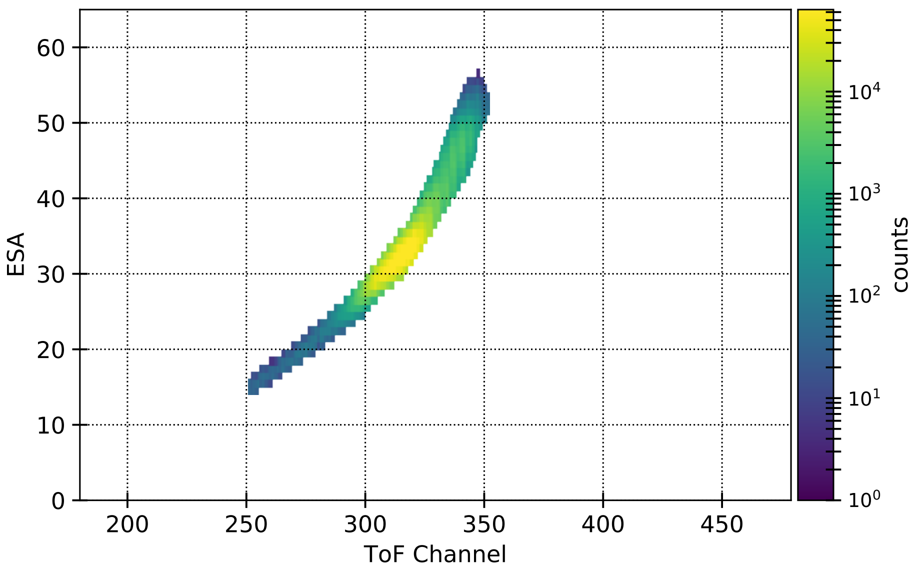

FIGURE 3.9: He^{+} (above) and He^{2+} (below) selections that have been cut out from fig. 3.8.

Chapter 4

Data Analysis

In Chapter 3 was described how an ion's m, mpq and v can be determined from the PHA data. In this chapter we want to go one step further and obtain the three-dimensional velocity $\vec{v}$ from v.
For this it is necessary to combine the PHA data with position and orientation information of the Ulysses spacecraft. Two different coordinate systems are utilized for that. They will be introduced in a first step.

4.1 Coordinate Systems

In the following analysis the SWICS PHA data will be connected to the position and orientation of the Ulysses spacecraft. For this two different coordinate systems are utilized.

4.1.1 Heliographic Coordinate System

Trajectory data from the Ulysses Final Archive (2008) is used in this work to describe Ulysses' orbit. In this data set, Ulysses' position is given in daily intervals and based on different coordinate systems, including the heliographic coordinate system in the B1950.0 epoch.
The heliographic (HG) coordinate system is a Cartesian Sun-centered system with the Sun's equatorial plane as a reference plane. Its x-axis is directed along the line of ascending node, which is the intersection line of the ecliptic and the solar equatorial plane. While the latter has an inclination of $i_{\odot} = 7.25°$ against the ecliptic (Fränz et al., 2002) the line of ascending node is at an ecliptic longitude of $\Omega_{\odot} \approx 75°$ relative to the First Point of Aries in 1950 (NASA HelioWeb, 2019). The z-axis of the HG coordinate system is directed along the Sun's spin axis (northward) and the y-axis completes the right-handed system.
In HG spherical coordinates the longitude φ_{HG} is defined to be 0° for directions along the x-axis and increases towards the y-axis. The latitude ϑ_{HG} is 0° for directions within the solar equatorial plane and $+90°$ for northward directions.
However, when working with the Ulysses trajectory data it was found that these data were given in spherical coordinates for which $\varphi_{HG} = 0°$ was towards $-105°$ ecliptic longitude relative to the First Point of Aries. This means that the Ulysses trajectory coordinate system is shifted 180° around the solar spin axis against the classical definition (s.a.).
In Fig. 4.1 Ulysses' spherical HG coordinates as well as its distance from the Sun are given over the time of the mission.

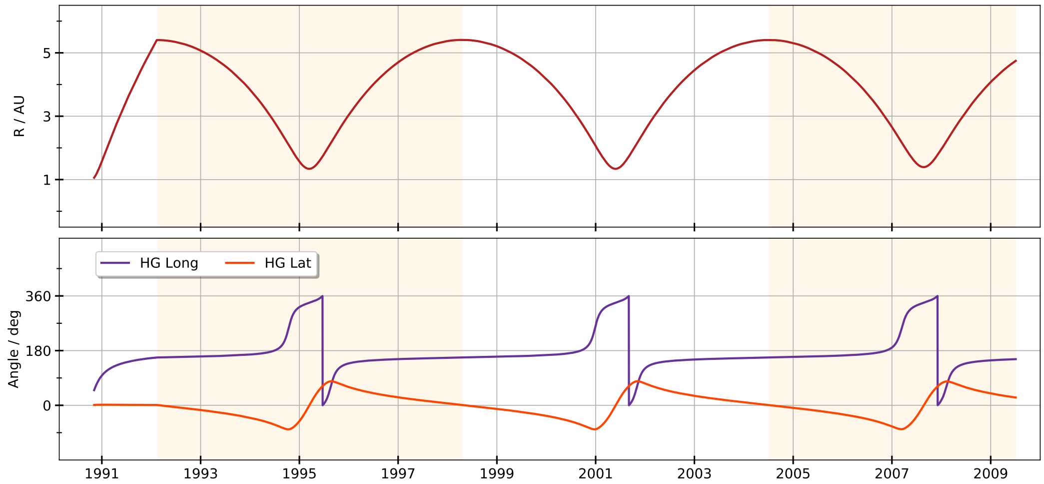

FIGURE 4.1: Ulysses trajectory data from November 1990 to June 2009 based on the data from the Ulysses Final Archive (2008). Color shaded are the three orbits of the mission. **Upper panel:** Shown is Ulysses' radial distance R from the Sun. Perihelion and aphelion of the spacecraft's elliptical orbit can clearly be seen as the nearest/farthest distance that is 1.3 AU and 5.4 AU. Over the duration of the mission Ulysses passes each of these points every 6.2 years and three times in total. **Lower panel:** Shown are Ulysses' HG longitude and latitude. Note that the longitude is shifted by 180° with respect to the classical definition (s. text for details). A clear periodicity over Ulysses' three orbits can be seen. Maximum and minimum latitude are $\sim \pm 80°$. These points are highest above the poles of the Sun and are reached a few weeks before and after Ulysses' pass through the perihelion.

4.1.2 Radial Tangential Normal Coordinate System

Ulysses' orbit has been described in the HG coordinate system, which is a coordinate system that is fixed with respect to the Sun. For describing positions and velocities in the frame of the spacecraft we need a coordinate system that moves with the spacecraft.

When dealing with Ulysses' trajectory data it is useful to work with Radial Tangential Normal (RTN) coordinates. The RTN coordinate system is defined relative to a moving object in the heliosphere, in this case Ulysses, and is centered at the Sun. A graphical representation of the system is given in Fig. 4.2. The unit vectors are $\vec{R}$, $\vec{T}$ and $\vec{N}$, where $\vec{R}$ points radially outward from the Sun to the current position of the spacecraft. $\vec{T}$ is defined as the normalized cross product of the Sun's angular velocity, $\vec{\omega}$, and $\vec{R}$. $\vec{N}$ completes the right-handed Cartesian coordinate system. Consequently, the RTN system is not defined for a spacecraft's position right above one of the Sun's poles as the cross product $\vec{\omega}$x$\vec{R}$ is zero here. Nevertheless we do not have to worry about this fact as Ulysses did not cross the poles directly.

4.2 The Detector Model

As described in Chapter 3, SWICS can distinguish between three different inflow directions of ions by the threefold division of solid-state detectors. A second directional information can be obtained by the rotation of SWICS being fixedly mounted

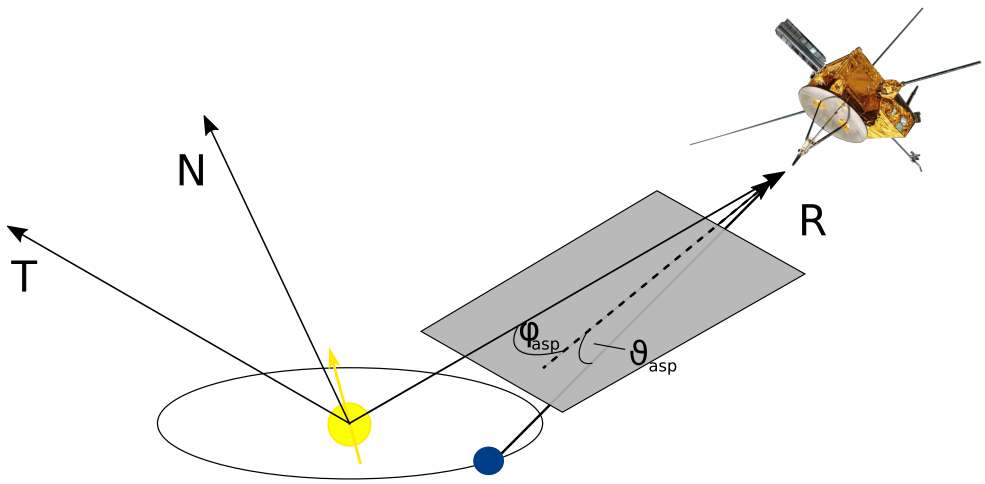

FIGURE 4.2: Graphical representation of the RTN coordinate system (not to scale). Shown are the Sun (yellow), the Earth (blue) and the Ulysses spacecraft at a non-specific position on its orbit. $\vec{R}$ is defined as the unit vector along the Sun–Earth line, $\vec{T}$ as the normalized cross product $\vec{\omega}$x$\vec{R}$ with $\vec{\omega}$ being the angular velocity of the Sun (yellow vector). $\vec{N}$ completes the right-handed Cartesian system. Also shown is the definition of the aspect angle components φ_{asp} and ϑ_{asp} as they are used in this work. The grey plane depicts the $\vec{R}$–$\vec{T}$ plane. $0° < \varphi_{\text{asp}} < 90°$ and $-90° < \vartheta_{\text{asp}} < 0°$ in the shown situation. The Ulysses Image is taken from European Space Agency, 2019 and modified.

on the spinning spacecraft as one spin of Ulysses is divided into eight sectors. These two additional measurements allow us to derive a three-dimensional velocity $\vec{v}$ of incident ions.

With each Triple Coincidence PHA word we receive information of which of the three solid-state detectors has been hit and in which of the eight sectors the measurement took place. However, a sector-detector information alone is not sufficient to determine the ion's three-dimensional velocity. Its meaning is highly dependent on SWICS' orientation and the eigen-velocity of the spacecraft. Additionally, SWICS' collimator is characterized by an intricate geometry, making an analytical solution of the problem difficult. Instead, we choose to use a virtual detector as a numerical approach. The initial idea of modelling the SWICS detector comes from Dr. Lars Berger who constructed a similar model for ACE SWICS. This work focusses on establishing the model for Ulysses SWICS.

4.2.1 Construction

For reconstructing the velocity space that is observed by SWICS we need to know the possible directions of incident particles that can enter the instrument. These directions are limited by the instrument's entrance system.

The original geometry of the SWICS entrance system was read out from a CAD model. To illustrate the intricate geometry, a photo of a 3D printed model of the entrance system is shown in Fig. 4.5.

The instrument is mounted with one of the collimator's narrow side edges parallel to Ulysses' spin axis. When we define this edge to be lying on the x-axis of a

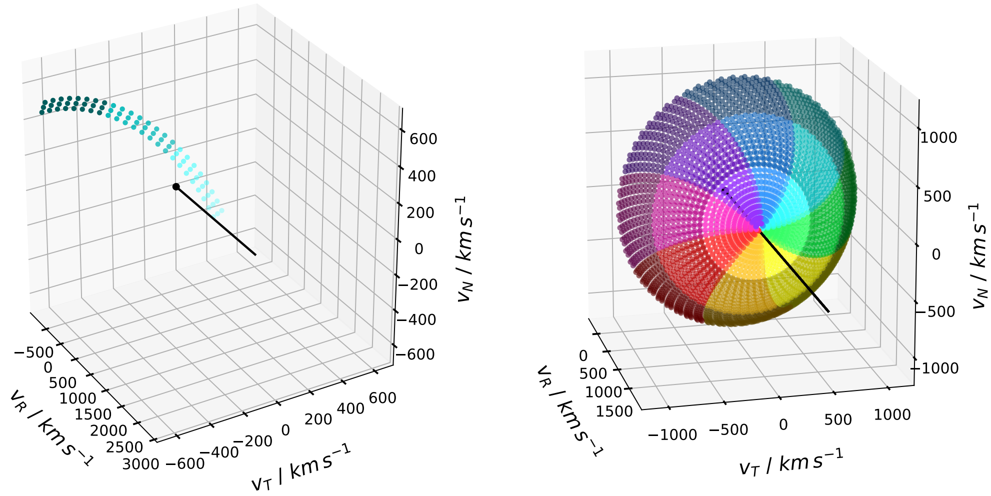

FIGURE 4.3: Velocity acceptance volume for ESA step 10 ($v \sim 1200\,\mathrm{km\,s^{-1}}$) For a fixed instrument (**left Panel**) and integrated over one spin that is divided into eight sectors (**right Panel**). The differently shaded areas indicate the acceptances of the three solid-state detectors. The black line shows the radial direction, i.e. velocities towards the Sun.

three-dimensional Cartesian coordinate system, the collimator geometry can be reconstructed by revolving this edge for 90° around a straight line that lies in the xy-plane with an angle of 56° relative to the x-axis. These 90° are divided into three parts, each of which is reserved as the opening angle for one of the three detector elements that are described in Sec. 3.2.

The detector's field of view is the solid angle over which the detector is sensitive to incoming particles. It can be represented by a set of outward directed normal vectors on the opening plane of the detector. In our model, we have a variable number n_d of these equidistant vectors which we can divide along the width and the height of the detector opening. The real continuous field of view is modelled better with an increasing number of normal vectors that cover the opening.
Each of these normalized vectors $\mathbf{f_i}$ has a unique direction $\mathbf{f_i} = \left[f_{x,i}\, f_{y,i}\, f_{z,i}\right]'$ in position space.
With a spin of the Ulysses spacecraft the fixedly mounted SWICS instrument is revolved around the spacecraft spin axis. One revolution of SWICS is divided up into eight sectors of approximately equal duration, each covering 45° (s. Sec. 3.3). As the spacecraft is spinning continuously, also the field of view changes its rotation angle continuously. For our virtual detector we model this by rotating the field of view gradually over n_sec steps through every sector.
The integrated field of view over one spin then comprises $n_\mathrm{FoV} = n_\mathrm{d} \cdot n_\mathrm{sec} \cdot 8$ single vectors $\mathbf{f_i}$ which are directed symmetrically around the spin axis.

From Field of View to Velocity Space

The detector's velocity acceptance can be calculated by combining the directional information from the field of view with the value of absolute velocity from the current ESA step.

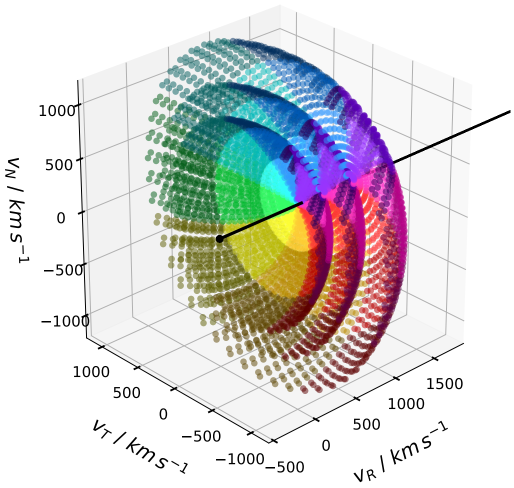

FIGURE 4.4: Velocity acceptance volume for three ESA steps 4, 10 and 17. Acceptance velocities on each shell have the same velocity v_i, i.e. the same distance to $v = 0\,\mathrm{km\,s^{-1}}$ (black dot) in this plot. v_i corresponds to the respective ESA step

Limited by the collimator, a particle can only enter the detector when its absolute velocity is within the acceptance of the current ESA step and when its velocity vector is antiparallel to the detector's field of view. For a given acceptance velocity v_i, each field of view vector $\mathbf{f_i} = \left[f_{x,i}\, f_{y,i}\, f_{z,i}\right]'$ can be associated with an acceptance velocity vector

$$\mathbf{v_i} = \begin{bmatrix} v_{R,i} \\ v_{T,i} \\ v_{N,i} \end{bmatrix} = - \begin{bmatrix} f_{x,i} \\ f_{y,i} \\ f_{z,i} \end{bmatrix} \cdot v_i. \tag{4.1}$$

The resulting acceptance of the fixed instrument for $n_d = 72$ and $v \sim 1200\,\mathrm{km\,s^{-1}}$ is shown in Fig. 4.3, left panel.
With consideration of the integrated field of view over one spacecraft spin the acceptance velocity for a distinct velocity v_i consists of the combination of n_{FoV} discrete velocities which form a dome with radius v_i in velocity space, s. Fig. 4.3, right panel, for $v \sim 1200\,\mathrm{km\,s^{-1}}$)

The central velocity for an ion of charge q and mass m at an ESA step with energy-per-charge EpQ (in keV/e) is

$$\frac{v_c}{km\,s^{-1}} = \sqrt{\frac{2 \cdot EpQ \cdot 1.602 \cdot 10^{-19} \cdot |q|}{m \cdot 1.661 \cdot 10^{-27}}}$$

with $m = 4\,\mathrm{u}$ and $|q| = 1\,\mathrm{e}$ for He^{+}.
Different absolute velocities v appear as distinct shells of radius v in velocity space. To get an idea of this, an example with three of those (ESA steps 4 ($v \sim 1480\,\mathrm{km\,s^{-1}}$), 10 ($v \sim 1190\,\mathrm{km\,s^{-1}}$) and 17 ($v \sim 930\,\mathrm{km\,s^{-1}}$)) shells is shown in Fig. 4.4.
To represent the uncertainty in the energy-per-charge measurement, we take into account the relative uncertainty $\Delta\frac{E}{q}/\frac{E}{q} = \pm 2.5\%$ (Gloeckler et al., 1992) and translate it into an uncertainty $\Delta v/v = \frac{1}{2}\left(\Delta\frac{E}{q}/\frac{E}{q}\right) = \pm 1.25\%$ in accepted velocity. For every

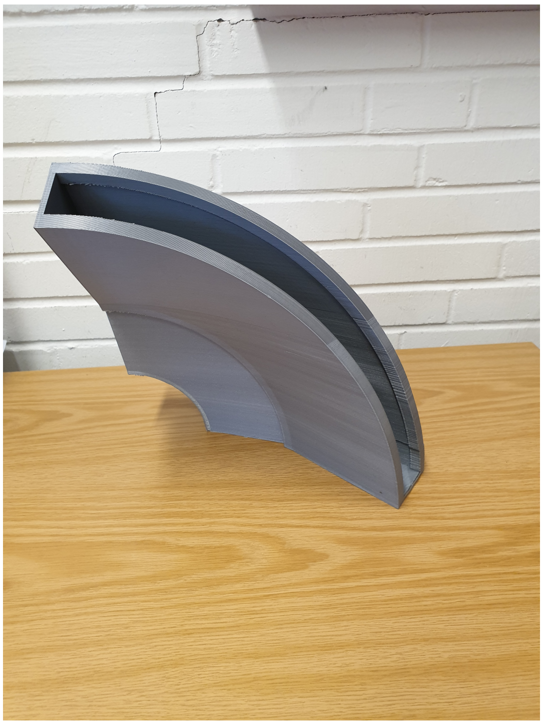

FIGURE 4.5: 3D printed model of SWICS' entrance system that was made from the original CAD files. Its geometry can be described by a cut of 90 ° longitude from a sphere at 56° polar latitude. The resulting piece is not flat but curved and has a height of $\sim$ 5 cm. This geometry leads to two deflection plates that are curved but have a constant distance of $\sim$ 3.7 cm over a relatively large area which is necessary to provide a constant voltage for the energy-per-charge filtering action (s. Sec. 3.2.1). The resulting opening angles of the collimator are 69° in width and 4° in height.

ESA step we can now choose a number of n_{epq} single velocities that are distributed evenly in the interval $[v_c - \Delta v/v, v_c + \Delta v/v]$.
By combining all $64 \cdot n_{epq}$ shells we obtain a dense three-dimensional pattern of accepted velocities that simulate the real continuous velocity acceptance volume of the spinning detector.

When we measure a PHA word with a distinct sector, detector and ESA information, we can now determine a set of three-dimensional velocities with which the particle could have entered the instrument. Of course, the resolution is limited as sector and detector areas are finite and because of the uncertainty $\Delta\frac{E}{q}/\frac{E}{q}$. By spreading the count over the entirety of $(n_i = n_{epq} \cdot n_{sec} \cdot n_d \cdot \frac{1}{3})$ absolute velocity acceptances in the volume of the sector-detector-ESA combination, we assign a set of equally likely possible velocities to the count.

4.2.2 Ulysses' Eigen-velocity

For the considerations in the previous section we assumed a detector on a spacecraft that is fixed in space. Obviously this is not the case for the Ulysses spacecraft, which moves on its elliptical orbit around the Sun. When considering a velocity measurement from a moving spacecraft, the actual velocity in an external frame of reference

is determined as an addition of the measured velocity and the spacecraft's eigen-velocity.
For determining the spacecraft's velocity we make use of the daily trajectory data from Sec. 4.1. For every point in time t_i we calculate the spacecraft's instantaneous velocity $v_{SC,i}$ by forming the differential quotient

$$v_{SC,i} = \frac{\begin{bmatrix} R_{i+1} \\ T_{i+1} \\ N_{i+1} \end{bmatrix}_i - \begin{bmatrix} R_i \\ T_i \\ N_i \end{bmatrix}_i}{t_{i+1} - t_i}$$

with t_{i+1} being the time of the next trajectory data given, which is normally $t_i + 1\,\mathrm{d}$. Note that the spacecraft's position at t_{i+1} has to be considered in the RTN coordinate system that relates to the spacecraft's position at t_i. The resulting velocities in RTN coordinates are shown in Fig. 4.6 and range between $-20\,\mathrm{km\,s^{-1}}$ and $35\,\mathrm{km\,s^{-1}}$.
To correct the measured velocities for the spacecraft's eigen-velocity, we add the resulting eigen-velocity components to the velocity acceptance. Thus, for every instant in time the shells in Fig. 4.4 are shifted a bit in velocity space based on the respective eigen-velocity.

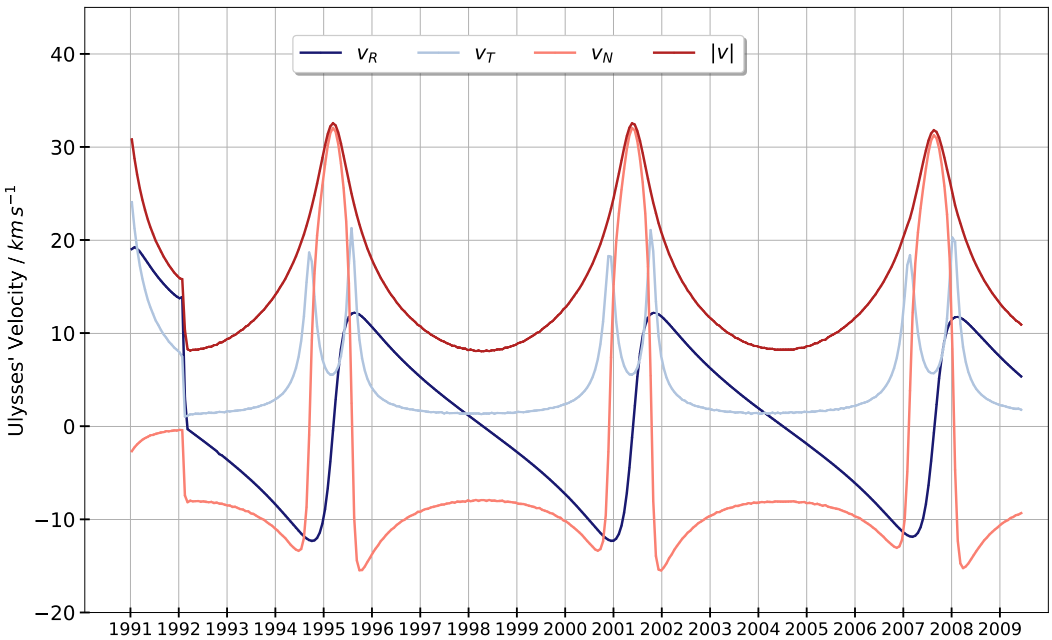

FIGURE 4.6: Eigen-velocity of Ulysses over the time of the mission. Shown are the RTN components and the absolute velocity.

4.2.3 Orientation of the Detector

Until now we have assumed that Ulysses' spin axis is aligned with the R-axis of the coordinate system, i.e. that the spin axis points directly to the Sun. In fact, this is not the case in general. Due to telemetry reasons, Ulysses' high gain antenna has to be oriented directly towards Earth. As Ulysses' spin axis is aligned with the electrical axis of the antenna (Wenzel et al., 1992), it has an offset towards the spacecraft-Sun line. This offset is called aspect angle and is a permanently changing quantity as a function of Ulysses' position and the position of the Earth. Because a varying aspect angle results in SWICS covering different parts of velocity space it is essential to consider this quantity in detail.

Calculation of the Aspect Angle

The aspect angle is measured from the Ulysses–Sun line to the Ulysses–Earth line. To describe this angle uniquely for any moment, we need two spherical coordinates φ_{asp} and ϑ_{asp} based on the RTN system. As shown in Fig. 4.2, φ_{asp} is measured in the $\vec{R}$–$\vec{T}$ plane between $-\vec{R}$ and the projection of the Ulysses–Earth line into this plane. φ_{asp} is $0°$ for directions along $-\vec{R}$, that is the Ulysses–Sun line, and increases to positive values towards $-\vec{T}$. ϑ_{asp} is the angle between the projection of the Ulysses–Earth line into the $\vec{R}$–$\vec{T}$ plane and the spin-axis. It is defined as $0°$ for directions that lie within the $\vec{R}$–$\vec{T}$ plane and $+90°$ for directions along $\vec{N}$.
For the calculation of the aspect angle we use the Ulysses trajectory data (s. Sec. 4.1) and Earth trajectory data in heliographic coordinates on a daily basis from NASA HelioWeb (2019) and converted both to RTN coordinates. In Fig. 4.7 both components φ_{asp} and ϑ_{asp} as well as the "flat" aspect angle α with $\alpha = \arccos(\cos\varphi_{\mathrm{asp}}) + \arccos(\cos\vartheta_{\mathrm{asp}}) - 1$ are shown over the time of the mission. φ_{asp} varies in the range from $\sim -25°$ to $\sim 42°$ and ϑ_{asp} in a range from $\sim -30°$ to $\sim 17°$. Large angles occur especially around the three fast latitude scans, i.e. when Ulysses is at its perihelion and has the smallest distance to Sun and Earth. The variable aspect angle is incorporated into the analysis by rotating the field of view corresponding to φ_{asp} and ϑ_{asp}. This results in a likewise rotation of the velocity acceptance space. In Fig. 4.8 the acceptance velocity for the ESA step 10 ($v \sim 1200\,\mathrm{km\,s^{-1}}$) is shown for $\varphi_{\mathrm{asp}} = 25°$ and $\vartheta_{\mathrm{asp}} = -10°$. Note that the orientation here seems to be mirrored with respect to the convention that has been described before. This is due to the inversion when transitioning from the field of view to velocity acceptance, s. Eq. 4.1.
When comparing Fig. 4.8 with Fig. 4.3, right panel, where a situation with $\vartheta_{\mathrm{asp}} = \varphi_{\mathrm{asp}} = 0$ is shown, it becomes clear that especially larger aspect angles change the link between a distinct sector-detector element and a volume in velocity space. While with a zero aspect angle a radial velocity (along $\vec{R}$) would be detected right in the middle of the velocity shell and definitely in the innermost detector, this is not the case for the aspect angle in Fig. 4.8. Here, an exclusively radially oriented velocity would be detected in a distinct sector in the central detector.
This also means that we can only transform a sector-detector measurement into a position in velocity space when we know about Ulysses' orientation!

Consistency Check

For checking if the considerations made before are reasonable and if the virtual detector works in the right way, we want to take a look at data of which we believe to know the velocity distribution function. Appropriate test data is the solar wind itself as it is believed to flow radially outwards from the Sun (Prölss, 2004, Ch. 6.1). An ideal candidate within the solar wind is He^{2+} as the most abundant species. We can identify He^{2+} easily in Fig. 3.8 and are provided with good statistics. Unlike protons, which are even more abundant in the solar wind, He^{2+} most likely deposits energy above the detector's threshold in the solid-state detector (s. Sec. 3.3.1). This is because of its higher mass and the twice as high charge, which leads to a higher

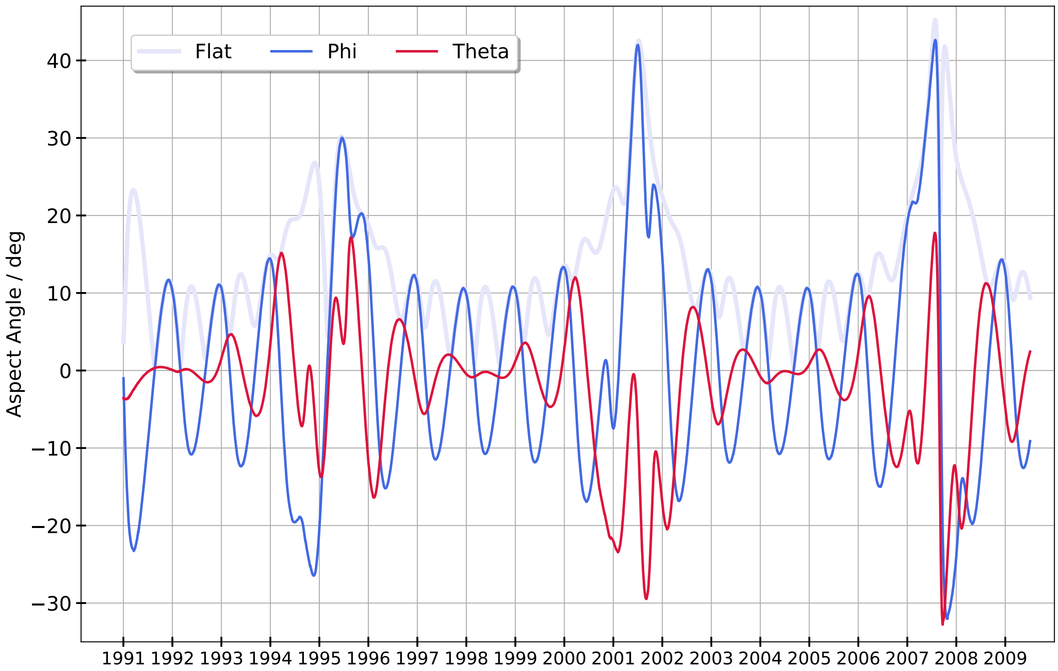

FIGURE 4.7: The evolution of Ulysses' aspect angle components φ_{asp} and ϑ_{asp} and the "flat" aspect angle α with $\alpha = \arccos(\cos\varphi_{asp}) + \arccos(\cos\vartheta_{asp}) - 1$ from 1991 to the end of the mission. The aspect angle is the angle between the Ulysses–Sun line and the orientation of Ulysses' spin axis. A constantly changing aspect angle results from the fact that the spacecraft's antenna, which is nearly parallel to the spin-axis, has to point towards Earth all the time. Particularly large aspect angles occur during the three fast latitude scans around 1995, 2001 and 2007. Here, Ulysses' distance to Sun and Earth is at a minimum.

gain in energy by the post acceleration. Only when a particle triggers an E_{SSD} measurement (Triple Coincidence) we get a directional information about its velocity. Protons are most often measured as Double Coincidences except for suprathermal protons, for which the assumption of radial streaming must not hold true. For selecting He^{2+} we proceed like described in Sec. 3.4.

In a first step we look at periods of time in which both aspect angle components φ_{asp} and ϑ_{asp} are small ($< \pm 5°$). For these PHA words we draw a histogram of their sector and detector information. The result can be seen in the left panel of Fig. 4.9. The histogram shows that mainly the innermost detector is hit. This is the expected behavior when we imagine the instrument on a spacecraft that points directly to the Sun. A radially streaming flow then hits the instrument's detector that is oriented sunwards, which does not change with the spin of the spacecraft. This result is also consistent with the detector model for $\varphi_{asp} = \vartheta_{asp} = 0$ which is shown in fig. 4.3. A radial stream can be represented here by the black line which cuts through the velocity shell in its center, the region of the innermost detector.
In a second step we examine a time period in which Ulysses had a substantial aspect angle. This is particularly the case for when Ulysses is near its perihelion, s. Fig 4.7. We choose for the second orbit, i.e. days 1-90 in 2001. For all He^{2+} PHA data from this time we again histogram sector and detector information, which is shown

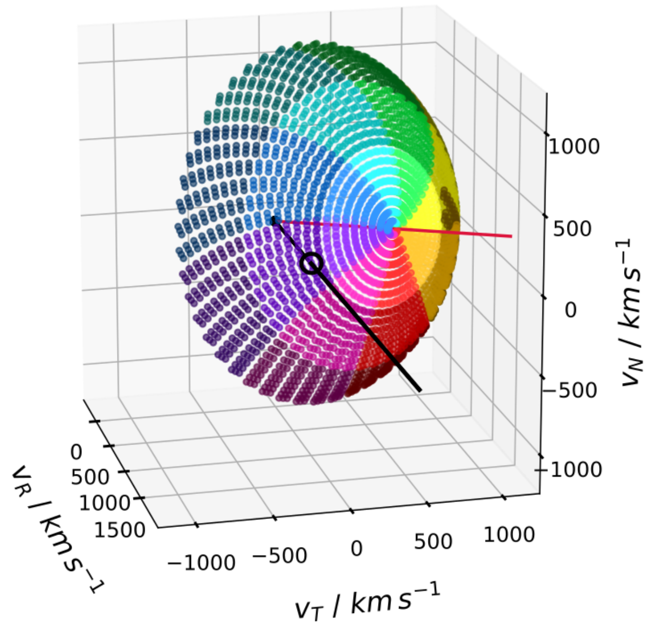

FIGURE 4.8: Velocity acceptance for ESA step 10 ($v \sim 1200\,\mathrm{km\,s^{-1}}$) and for aspect angles $\varphi_{\mathrm{asp}} = 25°$ and $\vartheta_{\mathrm{asp}} = -10°$. Ulysses' spin axis is drawn in red and the radial direction in black. Marked is also the sector-detector element in which an exclusively radial stream would be measured (black circle).

in the right panel of Fig. 4.9. Compared to the left panel the maximum of counts is now shifted clearly towards a single sector, that is Sector No. 4, and to the central detector. This is consistent with the virtual detector in Fig. 4.8, where the aspect angle's quantity matches the one in the selected time period. Counts do not show up exclusively with this single sector-detector combination but slightly spread out over adjacent sector-detector elements. This is due to the fact that solar wind He^{2+} does not stream as an ideal beam but has a certain temperature, i.e. width (Prölss, 2004, ch. 6.1).

Spin Reference Pulse

In the previous section it was observed that He^{2+} PHA counts accumulate around the central detector for large aspect angles. Still it needs to be examined how the sectors are oriented.

As mentioned before, one spacecraft spin is divided into 8 sectors, starting with sector 0 and ending with sector 7. Every spin's start is defined newly by the "spin reference pulse" of Ulysses (Hunt-Ward et al., 1999). This pulse is triggered by a combination of four sun sensors which detect when the Sun crosses a plane that is spanned by the spacecraft's spin axis and the spacecraft's x-axis, which is a particular axis perpendicular to the spin axis. The spin reference pulse is not uniform over time as the position of the Sun relative to the spacecraft changes with varying aspect angle.

To extract correct directional information from a sector data product of an ion that has been detected by SWICS it is essential to know the relative orientation between

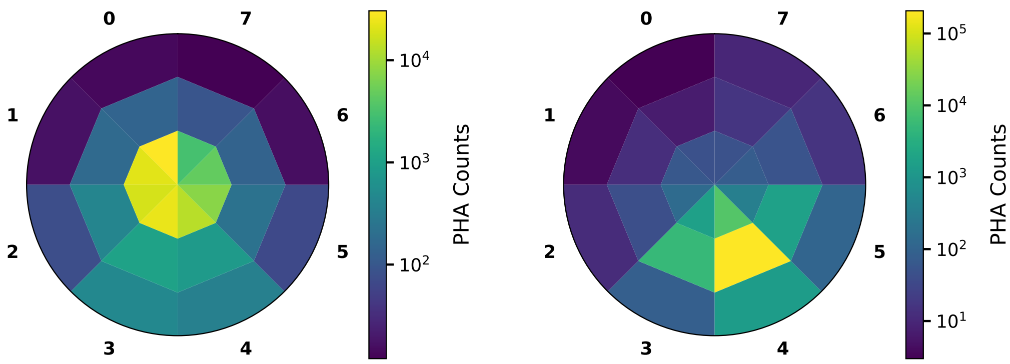

FIGURE 4.9: Histogrammed sector and detector information of PHA counts. **Left panel:** 365 days from 1992, φ_{asp} and ϑ_{asp} limited to angles $< \pm 5°$. **Right panel:** DOY 1-90 from 2001 (large φ_{asp} and ϑ_{asp}).

SWICS' main axis and the x-axis on the spacecraft. In the virtual detector this is implemented as an angle against the spacecraft–Sun line by which the field of view is rotated around the spin axis.
From the SWICS DPU (1988, p. 20-22) we know that the Sun pulse that triggers the beginning of Sector 0 is shifted by 180° against SWICS' main axis, i.e. on the opposite side of Ulysses spin axis. This means that the spacecraft has to rotate for half a spin after the sun pulse until SWICS measures particles streaming radially from the Sun. However, it was possible to set a fine adjustment which would lead to an offset of the sun pulse from this center line up to 22.5° SWICS DPU (1988, S.48). Unfortunately, we do not know the value that has been chosen.
If we assumed a wrong angle, a particle beam coming from a fixed direction in a Sun-fixed frame would be linked to a different direction. But this shift between true and supposedly measured direction is not constant over aspect angles. If we then measured over a longer time period with various aspect angles, we would measure the beam as blurred in velocity space.
To make sure our model uses the right angle, we again choose He^{2+} as a test population of which we assume a beam-like behaviour streaming radially from the Sun. Also, we can only look at time periods when the aspect angles were large and the maximum of He^{2+} counts occurs in the central or outermost detector. Only here we can clearly discriminate between single sectors. When measured in the innermost detector the slightly widened distribution of He^{2+} would spread across all sectors as they are close together here. From Fig. 4.9, right panel, where we histogrammed He^{2+} PHA words at a sizeable aspect angle, we find that the data is in agreement with the overall idea of a Sun pulse that is issued a half spin before SWICS faces the Sun. If we believe the assumption that He^{2+} streams radially from the Sun, Sector 4, that is shifted by 180° relative to Sector 0, contains the radial direction. To check for a potential fine adjustment we search for tendencies of the maximum of counts sweeping to an adjacent sector. However, such a tendency that is consistent over time cannot be found. Thus, we proceed the analysis with the assumption that no crucial fine adjustment had been set.

Transformation into w-space

With the considerations of eigen-velocity and orientation of Ulysses we can use the virtual detector for translating He^+ PHA words into the three-dimensional velocity space. Only when we have unfolded absolute velocities into its three components we can take the important step of transforming from a spacecraft frame of reference to a solar wind frame of reference.
Under the assumption that the solar wind streams basically radially this can be done by subtracting the instantaneous solar wind speed in R-component from a velocity in the spacecraft frame:

$$\mathbf{v_{i,sw}} = \begin{bmatrix} v_{R,i,sc} \\ v_{T,i,sc} \\ v_{N,i,sc} \end{bmatrix} - \begin{bmatrix} v_{sw} \\ 0 \\ 0 \end{bmatrix}$$

In a last step every component of the resulting vector is divided the by solar wind speed:

$$\mathbf{w_{i,sw}} = \begin{bmatrix} v_{R,i,sw}/v_{sw} \\ v_{T,i,sw}/v_{sw} \\ v_{N,i,sw}/v_{sw} \end{bmatrix}$$

By this, the transition from velocity space in the spacecraft frame to solar wind independent w space in solar wind frame of reference is made.

4.2.4 Velocity Space Coverage

When analyzing He^+ PUI w-spectra with Ulysses SWICS, several effects have to be considered that limit the observable part of the w-space. The most obvious restriction results from the fixed geometry of the collimator (s. Sec. 4.2.1)) which allows to observe only a dome-shaped part of the w-space when considering the spin of the spacecraft and varying ESA steps. (However, this dome is not fixed in w-space for different orientations of the spacecraft. While the ever changing aspect angle of Ulysses introduces a complex subject to directional data analysis it also enlarges the integrated coverage of velocity space over time.)
Furthermore, we have to deal with a limitation of the coverage in w_R-direction particularly for He^+ triple coincidences. The observable range in ESA steps is 19 to 0, which for He^+ corresponds to a limitation from $864\,\mathrm{km\,s^{-1}}$ to $1708\,\mathrm{km\,s^{-1}}$. While the upper limit is simply due to SWICS' highest possible ESA step, the lower limit is the lowest value for which He^+ still has enough energy to overcome the threshold of the solid-state detector and thus can trigger a valid energy measurement (s. Sec. 3.3.1).
The w-range that is consequently covered is highly dependent on the prevalent solar wind speed. For $v_{sw} = 700\,\mathrm{km/s}$ the absolute w in a spacecraft frame is limited to $1.2 < w_{SC} < 2.4$, whereas for slow solar wind at $v_{sw} = 300\,\mathrm{km/s}$ the limitation is $2.9 < w_{SC} < 5.7$. In Fig. 4.10 an exemplary w-space coverage for $v_{sw} = 700\,\mathrm{km/s}$ and no aspect angle is sketched.
As we do not expect to measure the bulk of He^+ at velocities $w_{SC} >> 2$, we are thus limited to time periods with fast solar wind.
In this work solar wind speed data is used that has been measured by the instrument SWOOPS (Solar Wind Observations Over the Poles of the Sun, Bame et al., 1992) on Ulysses.

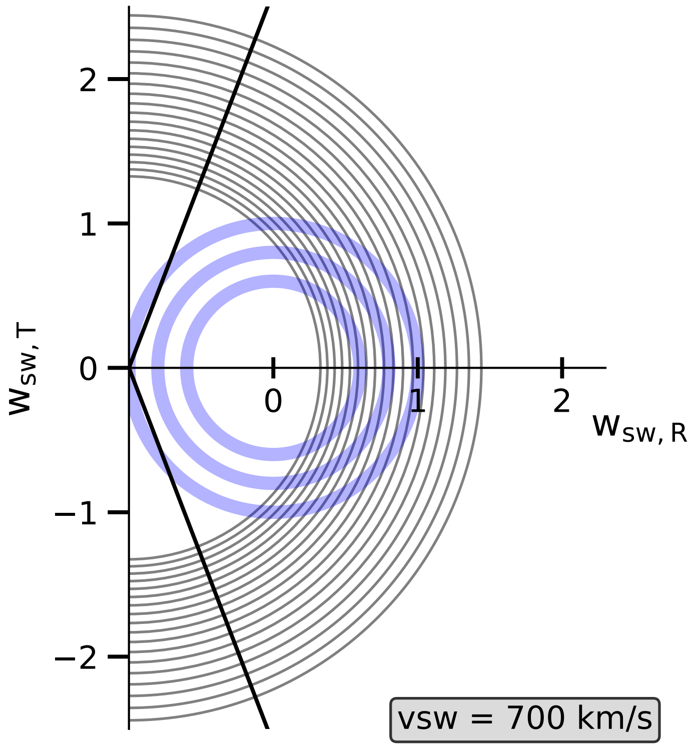

FIGURE 4.10: SWICS' 2D projected w-coverage for He^+ in the solar wind frame at solar wind speed 700 km s^{-1}. Only ESA steps 0-17 are covered. The black lines is the coverage due to the detector geometry. Circles of constant w in the solar wind frame are shown in blue for $w = 1$, $w = 0.8$ and $w = 0.6$.

In Fig. 4.11 a histogram for occurring solar wind speeds is shown – limited to times in which He^+ triple coincidences were measured. The number on the right indicates the total number of He^+ PHA triple coincidence data that was received within the year. One can see the overall variation of the solar wind speed that is due to different latitudes of the spacecraft: When close to the poles of the Sun, Ulysses is exposed to the fast solar wind (McComas et al., 2004), which is the case for example in 1995. Also, the total number of received data decreases heavily towards years in which Ulysses approaches the orbit's aphelion, e.g. 1998 at the end of the first orbit. This is mainly an effect of pickup ion flux reduction that scales with $r_\odot^{-2}$ due to the expansion of the solar wind (Prölss, 2004, ch. 6.1).

4.2.5 Phase Space Normalization

We are now able to combine the information about sector, detector and ESA step from the selected He^+ PHA triple coincidences with the information about how the spacecraft was moving and which direction it was facing at the time of the measurement. Counts that we have collected over a certain time period can be mapped into three-dimensional w-space by this. However, for deriving physical quantities from these, a transition from counts to phase space density has to be performed.

Firstly, we consider a single spin of the spacecraft, which normally corresponds to

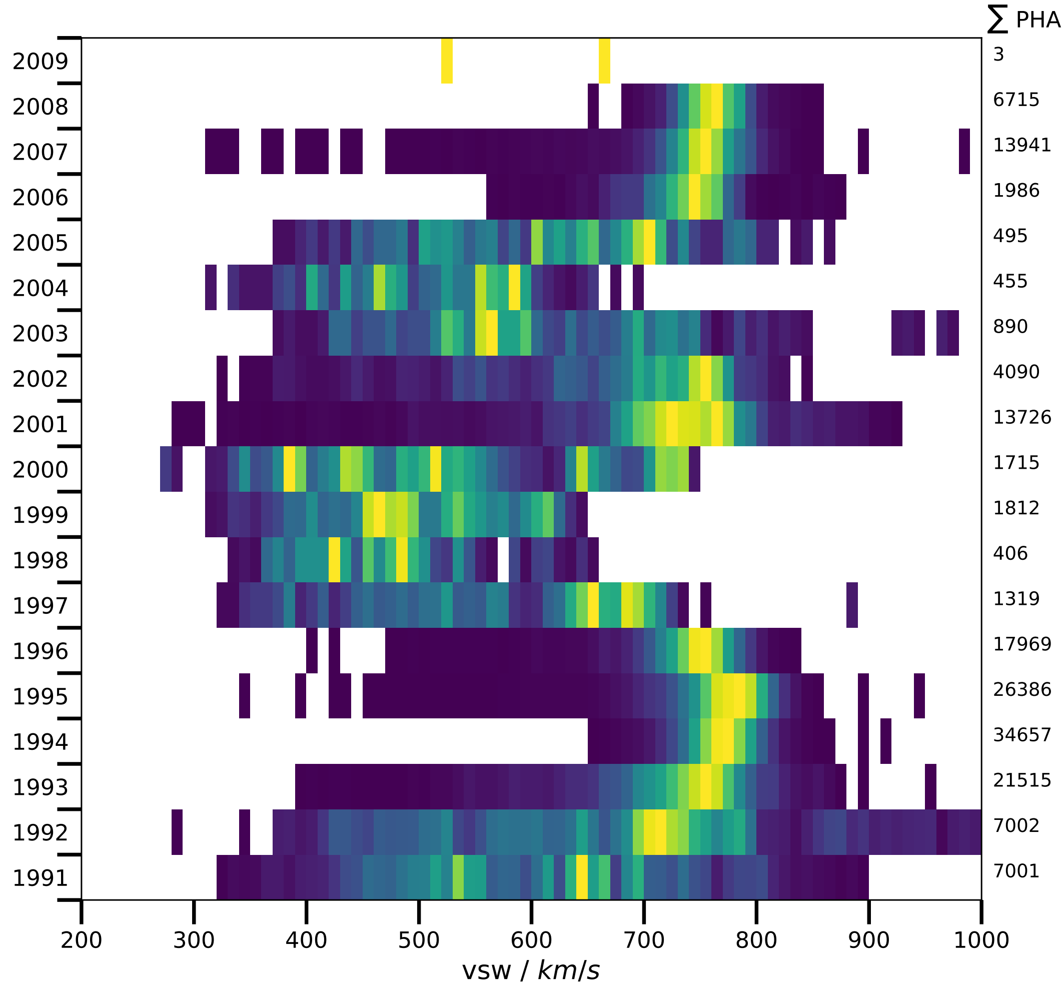

FIGURE 4.11: Histogram of solar wind speed measured by SWOOPS for times in which He^+ PHA data is measured by SWICS, sorted by years of the Ulysses mission. The color code is normalized to each year's maximum value (in yellow). In the right column one can find the total number of He^+ PHA words per year.

one ESA step of SWICS. Counts N_{jk} that have been measured in a phase space volume that has been covered by a sector-detector element j during the ESA step k can be connected to the average phase space density δ_{jk} in this volume by an integration over the three-dimensional velocity space:

$$N_{jk} = \iiint_{v_{\varphi j} v_{\vartheta j} v_{Rk}} \rho_{jk} V_k \, d^3 v,$$

where $V_k = G \, \tau \, v_k$ is the spatial volume of the measurement with the geometrical factor $G = 0.0225\,\mathrm{cm}^2$ (Dr. Lars Berger, personal communication), $\tau = 12/8\,\mathrm{s} = 1.5\,\mathrm{s}$, the time of the measurement in a single sector and v_k the central velocity for He^+ in the ESA step k. With the opening angles of a single sector-detector element of 4° in width and $69^\circ/3 = 23^\circ$ in length and the height of this element Δv_k we can write

$$N_{jk} = v_k^2 \left(\frac{\pi^2}{180^2} \cdot 4 \cdot 23 \right) \Delta v_k \, \rho_{jk} \, G \, v_k \, \tau.$$

Δv_k is determined by the uncertainty in energy-per-charge measurement. It has been found to be $\Delta v_k = 0.0125 \, v_k$ in Sec. 4.2.1, which gives us

$$N_{jk} = v_k^4 \left(\frac{\pi^2}{180^2} \cdot 4 \cdot 23 \right) 0.025 \, \rho_{jk} \, G \, \tau.$$

This we can be rewritten as an expression for the average phase space density δ_{jk} with the phase space volume V_k as

$$\rho_{jk} = \frac{N_{jk}}{V_k}.$$

Note that V_k is only dependent on the ESA step k, as the sector-detector elements span the same (absolute) phase space volume for one step.
When we want to measure more than one spin, we need to consider that the probability to detect an ion is dependent on the ESA step. This behaviour is described in Sec. 3.3.1 as the detection efficiency.
For phase space normalisation this is considered by weighting the spanned phase space volume for every sector detector element with the efficiency of the respective ESA step eff_k:

$$\rho_{jk} = \frac{N_{jk}}{V_k \cdot \mathrm{eff}_k}$$

To consider the resolution of the single sector-detector-ESA elements (s. Sec. 4.2.1) we assign each of the velocity acceptances in an element the count rate $\frac{1}{n_i} N_{jk}$ and the partial phase space volume $\frac{1}{n_i} V_k$.
As we will not always have counts in every scanned phase space volume, we have to integrate over longer periods of time to determine a phase space density. As the instrument covers different phase space volumes with varying aspect angle, changing parts of phase space volume are covered. To take this into account we have to divide the integrated count rate in a distinct volume by the integrated volume over all time in which this volume has been observed – independent on whether a PHA word has been measured.

Chapter 5

Results

Here we present first results of the method that has been developed in chapter 4 for He^+. For creating three-dimensional velocity spectra from He^+ SWICS PHA data we synchronize the selected data (s. 3, He^+ Triple Coincidences) with the spacecraft's aspect angle, its eigen-velocity and the present solar wind speed. This gives us directionally resolved counts from the observed phase space volume.

An example for data of a measuring period of 50 days in 1993, limited to solar wind speeds from 760 km s^{-1} to 780 km s^{-1}, is shown in Fig. 5.1. Here we histogrammed the counts by utilizing Cartesian $w_{\mathrm{sw,R}}$, $w_{\mathrm{sw,T}}$ and $w_{\mathrm{sw,N}}$ bins in solar wind frame. Shown are counts from a "slice" in the $w_{\mathrm{sw,T}} - w_{\mathrm{sw,N}}$ plane. Counts within the range $0.3 <= w_{\mathrm{sw,R}} < 0.5$ have been summarized for each $w_{\mathrm{sw,T}} - w_{\mathrm{sw,N}}$ bin. The orientation of this cut is sketched in Fig. 5.2 for better understanding.

By dividing these counts by the integrated phase space volume (PSV) for the ob-

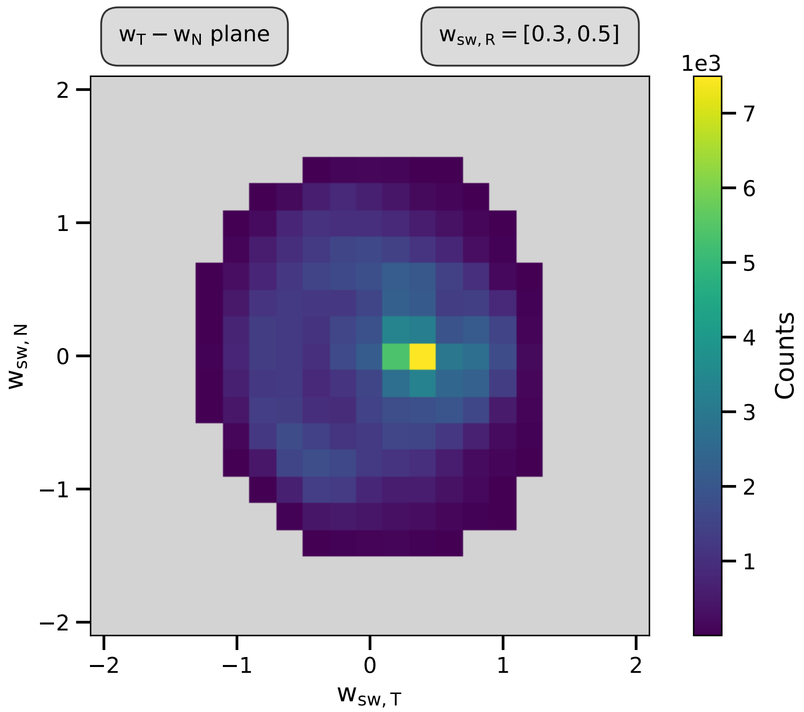

FIGURE 5.1: Cartesian cut through He^+ count distribution in a 3D w_{sw}-space, measured during DOY 315-365 in 1993 for solar wind speeds from 760 km s^{-1} to 780 km s^{-1}.

served time, which is binned in the same way and shown in Fig. 5.3, we yield the resulting phase space density (PSD), s. Fig. 5.4. When comparing the three Figures

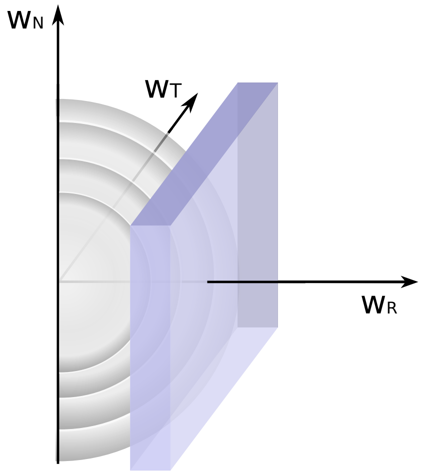

FIGURE 5.2: Sketch of the orientation of a slice in the $w_T - w_N$ plane. A selection of ESA shells is shown in grey.

5.1, 5.3 and 5.4 one can see a clear difference in overall shape between PSV and PSD (resp. counts). The nonzero part of the PSD does not cover all of the scanned PSV. This means that SWICS did not observe He^+ PUI over all of the observed PSV but only in a distinct partial volume.

However, the 2D projection of the PSD has a roundish shape. In fact we even find a spherical shape in 3D. As a feasible visualization a stepwise sequence of $w_{\mathrm{sw,T}} - w_{\mathrm{sw,N}}$ "slices" is displayed in the appendix A. Each slice is again a projection of the PSD from a width $\Delta w_{\mathrm{sw,R}} = 0.2$. The sequence starts with $w_{\mathrm{sw,R}}$-values below solar wind speed with the slice $-0.5 <= w_{\mathrm{sw,R}} < -0.3$ and steps seamlessly up to $1.1 <= w_{\mathrm{sw,R}} < 1.3$ in nine increments. The radius of the projection increases slightly towards $w_{\mathrm{sw,R}} \approx 0$ and then starts decreasing again for larger $w_{\mathrm{sw,R}}$. This suggests the three-dimensional shape of a sphere centered around $w_{\mathrm{sw,R}} = 0$, which is a finding that confirms the theory of an isotopic and cooled PUI VDF (s. Sec. 2.3). For $w_{\mathrm{sw,R}} < 0$ and towards smaller values of $w_{\mathrm{sw,R}}$ an increasing "hole" in the PSD emerges from the center. This is due to the fact of a limited instrumental coverage for He^+ at higher ESA steps, which is described in more detail in Sec. 4.2.4.

Apart from taking slices from the $w_{\mathrm{sw,T}} - w_{\mathrm{sw,N}}$ plane along the $w_{\mathrm{sw,R}}$-axis we can also cut the three-dimensional distribution of the PSD along the other two axes. This is shown for the $w_{\mathrm{sw,R}} - w_{\mathrm{sw,N}}$ plane in Fig. 5.5 and for the the $w_{\mathrm{sw,R}} - w_{\mathrm{sw,T}}$ plane in Fig. 5.6, each projection containing $w_{\mathrm{sw,R}} = 0$. Both images confirm the underlying three-dimensional spherical distribution.

Taking a look at the $w_{\mathrm{sw,R}}$-slice of the PSD in Fig. 5.4 again, one sees a relatively sharp peak in the bins around $w_{\mathrm{sw,T}} = 0.4$ and $w_{\mathrm{sw,N}} = 0$. This means that this part of PSV has been observed more often than surrounding parts, which is due to the spacecraft having a substantial aspect angle φ_{asp} at the end of the year 1993 (s. Fig. 4.7). Because the spacecraft's spin axis was tilted away from the radial direction for most of the time, this peak is shifted a little bit away from the center. The fact that this distinct part of PSV has been observed particularly often is followed by a qualitatively similar peak in counts, s. Fig. 5.1. As this peak is a result of the measurement and not a feature in the velocity distribution of He^+, it vanishes with the normalization process. The PSD shows an increased density over a wider range around the radial direction, which tells that He^+ tends to stream radial in this example from 1993.

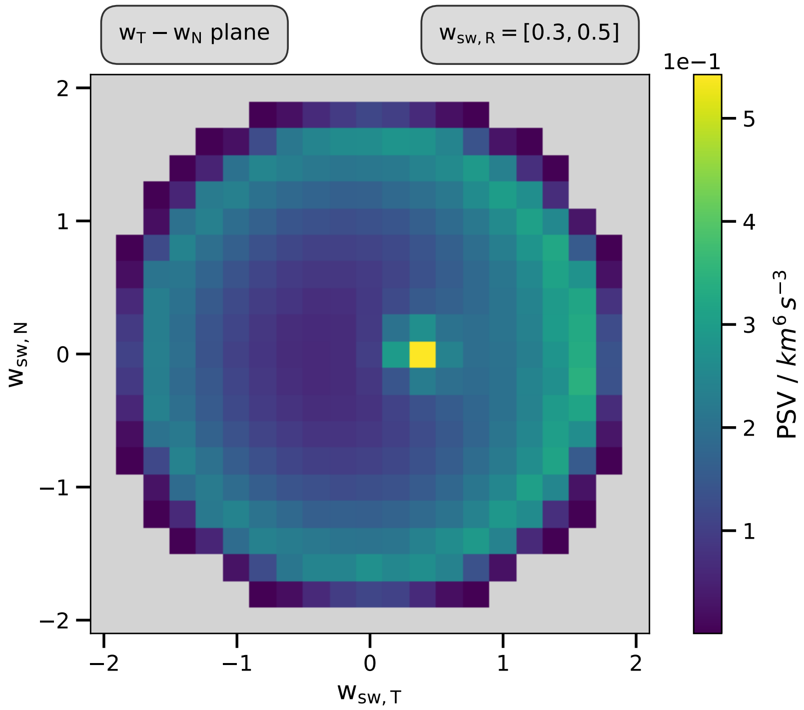

FIGURE 5.3: Cartesian cut through the integrated observed PSV in a 3D w_{sw}-space, measured during DOY 315-365 in 1993 for solar wind speeds from 760 km s^{-1} to 780 km s^{-1}.

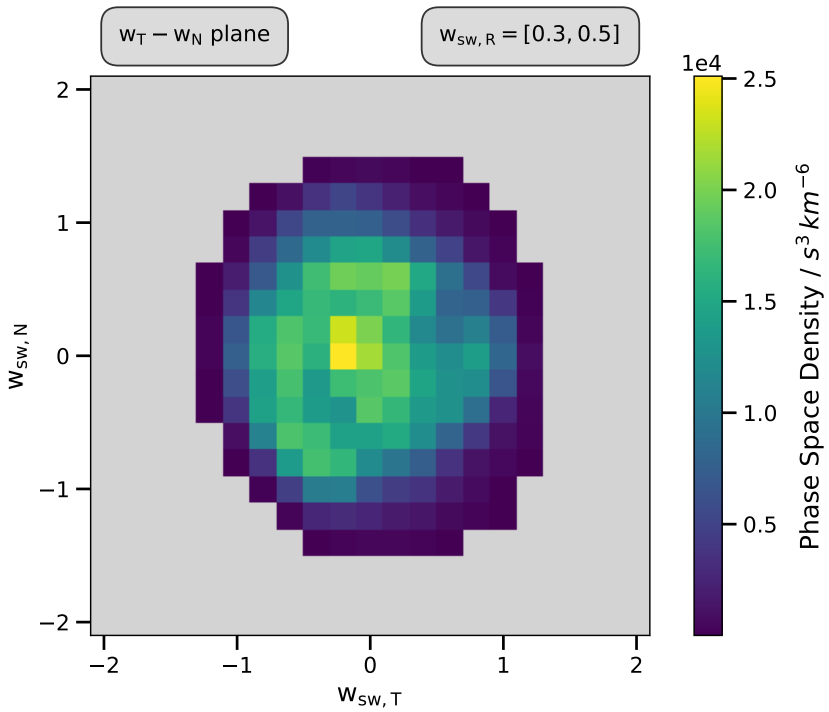

FIGURE 5.4: Cartesian cut through the three-dimensional PSD for He$^+$, measured during DOY 315-365 in 1993 for solar wind speeds from 760 km s^{-1} to 780 km s^{-1}

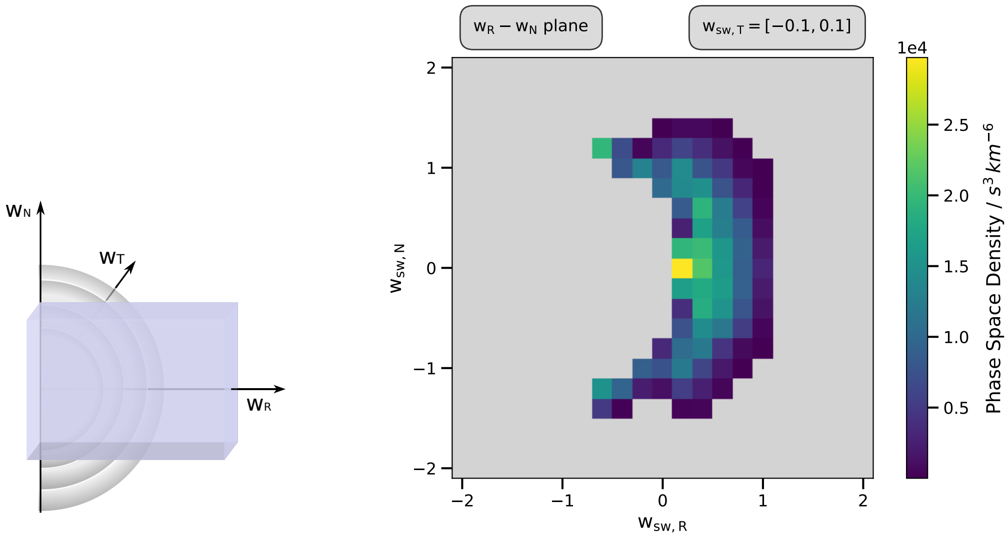

FIGURE 5.5: **Left:** Sketch of the orientation of a slice in the $w_R - w_N$ plane. A selection of ESA shells is shown in grey.
Right: Cartesian cut through the three-dimensional PSD for He^+, measured during DOY 315-365 in 1993 for solar wind speeds from 760 km s^{-1} to 780 km s^{-1}. The crescent shape results from SWICS' coverage.

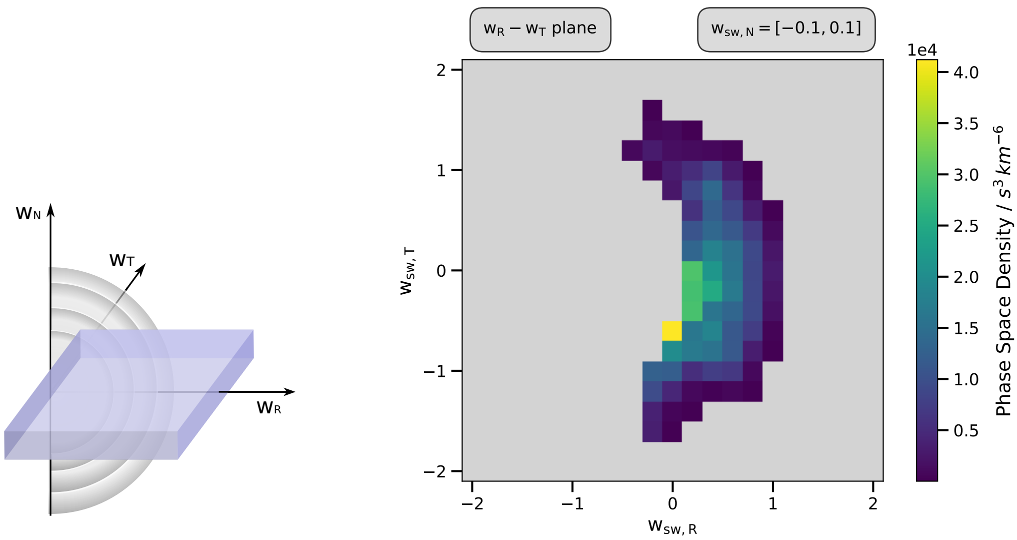

FIGURE 5.6: **Left:** Sketch of the orientation of a slice in the $w_R - w_T$ plane. A selection of ESA shells is shown in grey.
Right: Cartesian cut through the three-dimensional PSD for He^+, measured during DOY 315-365 in 1993 for solar wind speeds from 760 km s^{-1} to 780 km s^{-1}. The crescent shape results from SWICS' coverage.

In Fig. 5.9 we show the PSD for another longer time period of 250 days in 1994 at solar wind speeds 740 km s^{-1} to 780 km s^{-1} for a slice $0.1 <= w_{\text{sw,R}} < 0.3$. Corresponding Counts and PSV are shown in Fig. 5.7 and 5.8. Here, the counts show a ring structure which vanishes by normalization. The PSD in Fig. 5.9 shows distribution similar to the PSD from the shorter time period in 1993, concentrated and symmetrical around the central radial direction.

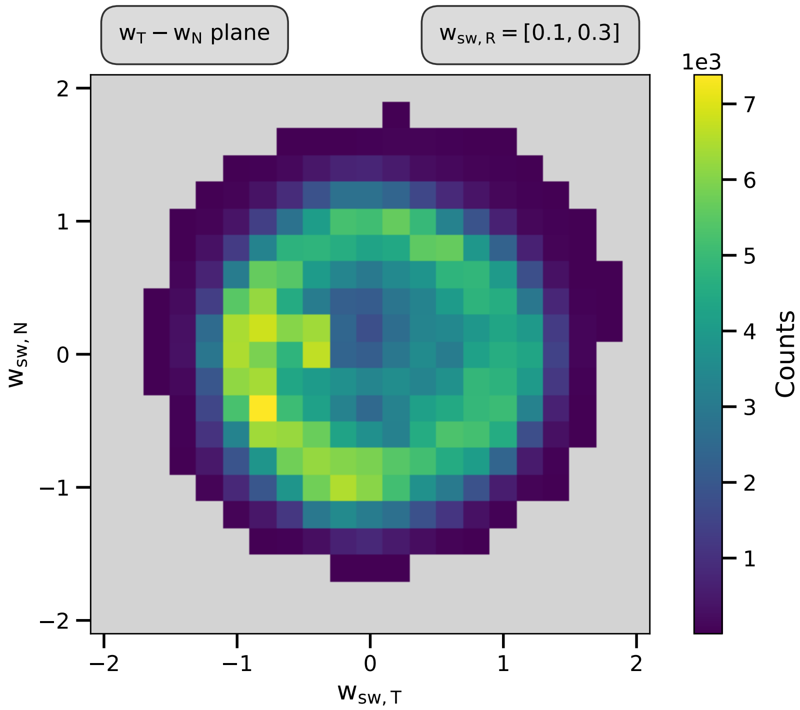

FIGURE 5.7: Cartesian cut through He$^+$ count distribution in a 3D w_{sw}-space, measured during DOY 1-250 in 1994 for solar wind speeds from 740 km s^{-1} to 780 km s^{-1}.

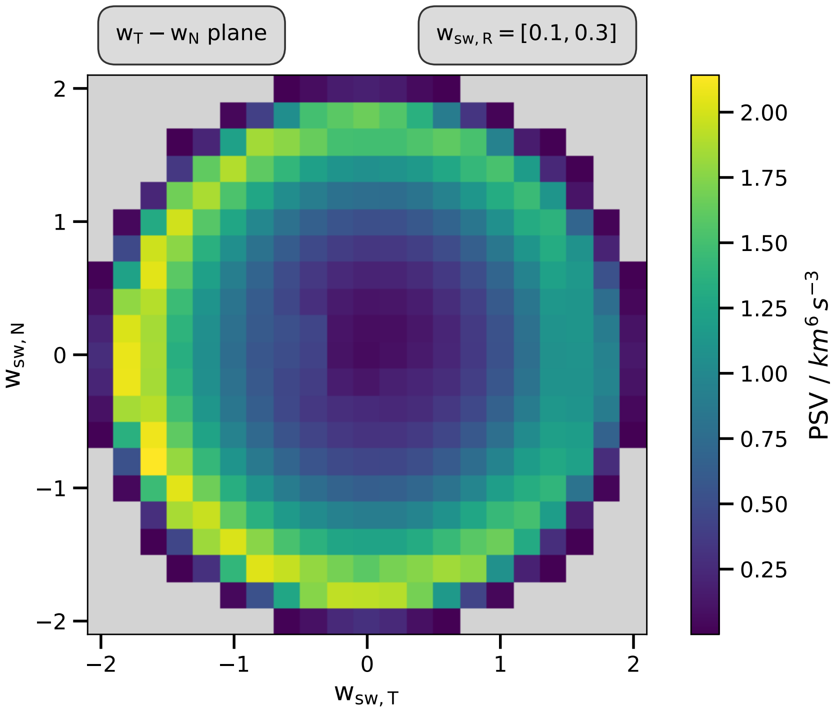

FIGURE 5.8: Cartesian cut through the integrated observed PSV in a 3D *w*sw-space, measured during DOY 1-250 in 1994 for solar wind speeds from 740 km s^{-1} to 780 km s^{-1}.

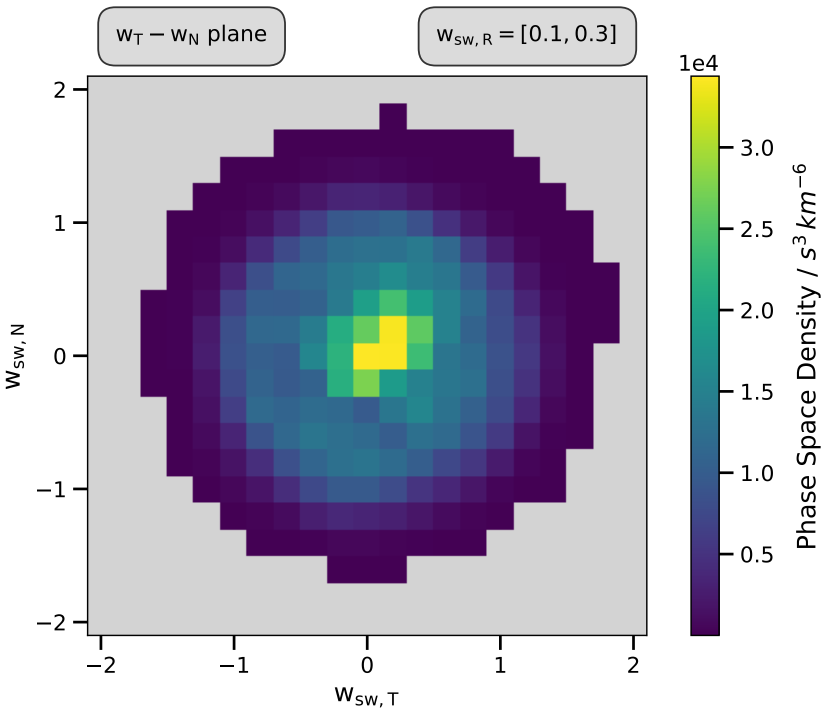

FIGURE 5.9: Cartesian cut through the three-dimensional PSD for He^+, measured during DOY 1-250 in 1994 for solar wind speeds from 740 km s^{-1} to 780 km s^{-1}

5.1 Spherical Projection

Of course we are not limited to the presented Cartesian projections. We can also choose a shell-wise projection. For this we consider spherical shells of constant $w$sw in the solar wind frame. For better understanding we can refer to Fig. 4.10 again. Here we see the blue rings as 2D cuts through such concentric shells around $w$sw $= 0$. The spherical coordinate φ is measured within the $w_{\mathrm{sw,T}} - w_{\mathrm{sw,N}}$ plane with $\varphi = 0°$ for $w_{\mathrm{sw,T}} = 0$ and $\varphi > 0°$ for negative values $w_{\mathrm{sw,T}}$. The second coordinate ϑ is defined perpendicular to the $w_{\mathrm{sw,T}} - w_{\mathrm{sw,N}}$ plane. It is $\vartheta = 0°$ for values within the plane and $\vartheta = 90°$ along the positive $w_{\mathrm{sw,N}}$ axis (out of the paper plane). In Figs. 5.10 and 5.11 we show counts and integrated PSV in this projection for He^{+} measurements from 50 days in 1993, restricted to solar wind speeds from 760 km s^{-1} to 780 km s^{-1}. The selected spherical shell comprises absolute w-values $0.85 <= w_{\mathrm{sw}} < 0.95$. Considering the definition of the two coordinates φ and ϑ we find, that the central viewing direction against the $w_{\mathrm{sw,R}}$ axis in Fig. 4.10. Even more clearly than in the Cartesian projection sharp peaks around $\varphi = 30°$ and $\vartheta = 0°$ are apparent in both figures 5.10 and 5.11, which is due to the variation in observation time of PSV. The histogram of the corresponding PSD, that excludes this effect, is shown in Fig. 5.12.
This spherical projection can become particularly suitable for the examination of the level of isotropy within a w_{sw}-shell. Shapes like a torus distribution (s. Sec. 2.3) can be observed directly. For a completely isotropized shell we would expect an evenly colored projection in Fig. 5.12. This is obviously not the case. Here, we find a structure of increased PSD that is around $-60\,°$ longitude for $\vartheta = 0\,°$ and moves towards $\varphi = 0\,°$ for higher latitudes.
Unfortunately, we could not find clear structures that were constant over different periods of measurement. A possible reason for that could be that we could only very vaguely determine the detection efficiency in Sec. 3.3.1. As the spherical projection comprises measurements from different ESA steps (s. 4.10), an inaccurate efficiency weighting could either lead to a disappearance of real structures or even to an emerging of artificial ones. A detailed analysis of the detection efficiencies as it is shown in Köten (2009) for ACE/SWICS is beyond the scope of this work but would be highly beneficial for future analyses.

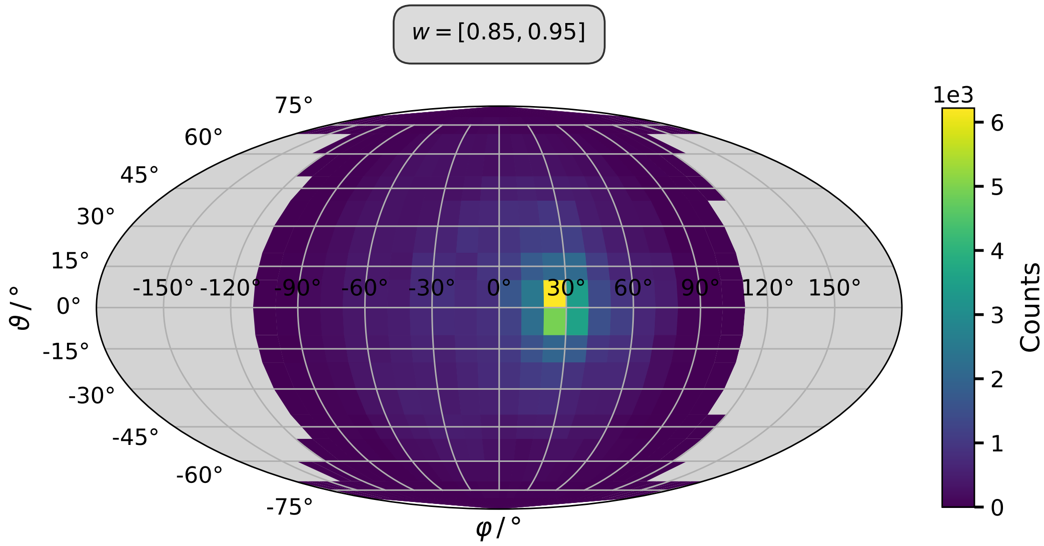

FIGURE 5.10: Spherical projection of He^{+} count distribution in a 3D w_{sw}-space, measured during DOY 315-365 in 1993 for solar wind speeds from 760 km s^{-1} to 780 km s^{-1}. Grey areas depict PSV that has not been observed and result from SWICS' coverage.

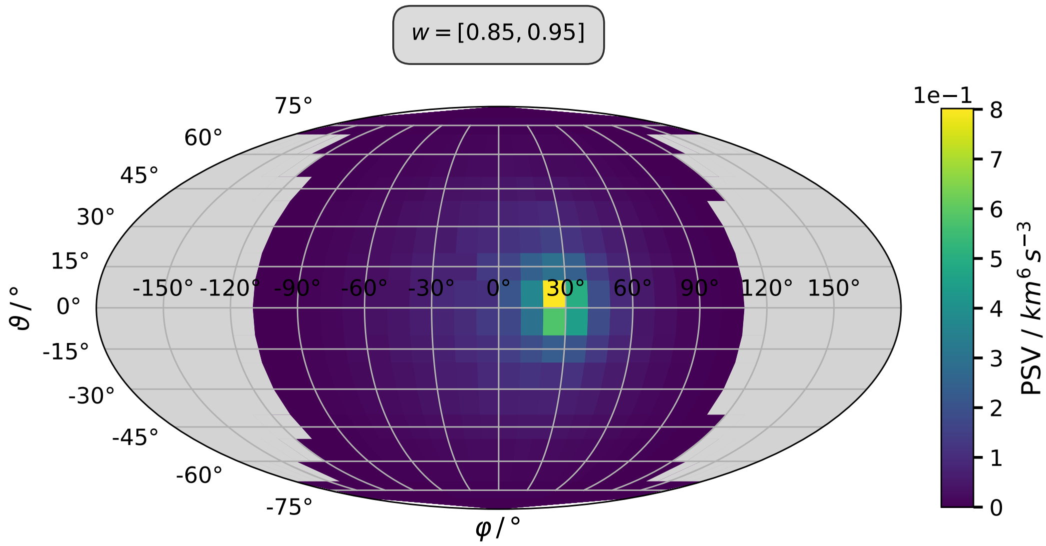

FIGURE 5.11: Spherical projection of the integrated observed PSV in a 3D w_{sw}-space, measured during DOY 315-365 in 1993 for solar wind speeds from 760 km s^{-1} to 780 km s^{-1}. Grey areas depict PSV that has not been observed and result from SWICS' coverage.

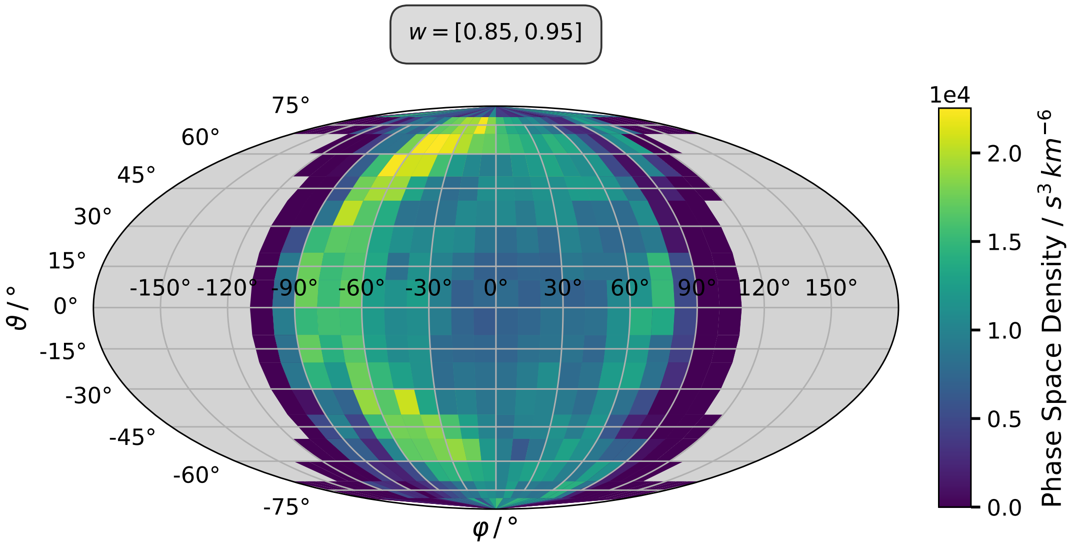

FIGURE 5.12: Spherical projection of the three-dimensional PSD for He^{+}, measured during DOY 315-365 in 1993 for solar wind speeds from $760\,\mathrm{km\,s^{-1}}$ to $780\,\mathrm{km\,s^{-1}}$. Grey areas depict PSV that has not been observed and result from SWICS' coverage.

5.2 1D Projection

In this last section we show 1D projections of three-dimensional velocity distributions from measurements of two different years. In each year (1994, 1996) we analyzed He^+ data from 100 days at solar wind speeds from $760\,\mathrm{km\,s^{-1}}$ to $770\,\mathrm{km\,s^{-1}}$. For this projection we integrate both the counts and the PSV over spherical shells around $w_{sw} = 0$. In a 2D cut this can be visualized by an integration along a blue circle in Fig. 4.10. We combined values within the width $\Delta w_{sw} = 0.1$ at different radii from $w_{sw} = 0.25$ to $w_{sw} = 1.05$. In Fig. 5.13 the histogram of the resulting PSD is shown. The histograms look qualitatively similar for both years. We see a relatively broad distribution with a clear cutoff around $w = 1$, which corresponds to $w_{sc} = 2$ (s. Sec. 2.3, Ch. 1). For smaller values of w_{sw} the distribution does not change over many magnitudes.
The spectra in Fig. 5.13 are also in good qualitative agreement with the one in Fig. 1.1. It should be noted that our spectra are limited to values $w_{sw} > 0.25$, while the spectrum in Fig. 1.1 is continued down to values $w_{sc} < 1$, which corresponds to values $w_{sw} < 0$ in solar wind frame. In Sec. 4.2.4 we have seen that He^+ Triple Coincidences can only be measured for distinct w-values above a limit that is dependent on the solar wind speed but hardly smaller than $w_{sw} = 1$. This shows that the spectrum in Fig. 1.1 is not based on solely Triple Coincidences but also on He^+ Double Coincidences. As Double Coincidences lack an energy measurement in the solid-state detector and thus a directional resolution, the spectrum can only result from an integration along different ESA shells that is projected onto a distinct possible value. Although the spectra look similar we want to emphasize that the spectrum in Fig. 5.13 results from a very different approach as we show projected cuts through an actual three-dimensional velocity distribution.

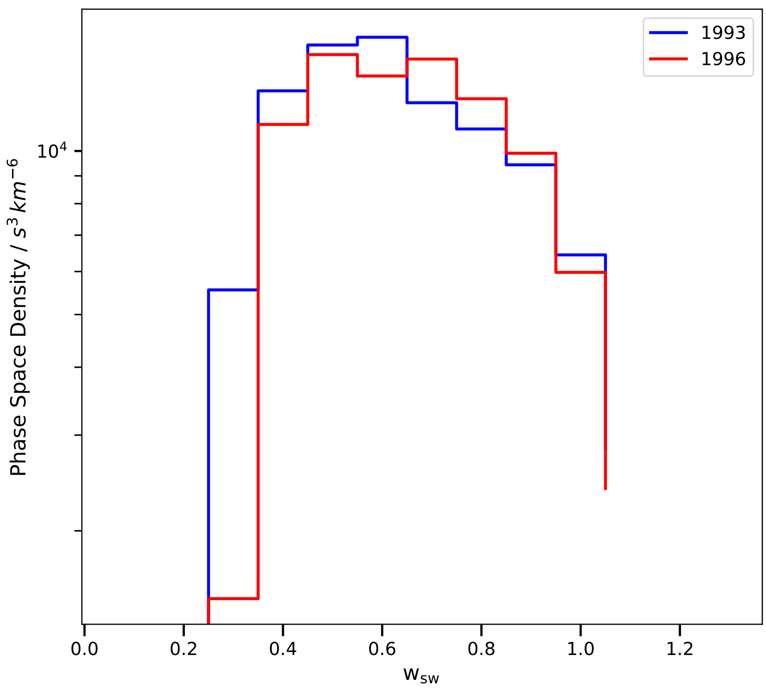

FIGURE 5.13: 1D projected PSD from a 3D w_{sw}-space, measured during DOY 1-100 in 1994 and 1996 for solar wind speeds from $760\,\mathrm{km\,s^{-1}}$ to $770\,\mathrm{km\,s^{-1}}$

Chapter 6

Summary and Outlook

The aim of this work was to prepare a tool for resolving ion measurements by Ulysses/SWICS in three dimensions and to apply this tool using He+ PUI.
In a first step He+ data was selected from the raw Ulysses SWICS PHA data. He+ events were identified by analyzing SWICS' combined measurements of energy-per-charge, time-of-flight and residual energy.
In a second step a model of the SWICS detector was developed, which allows us to translate the PHA data into three-dimensional velocity components. Here the key point was to combine the PHA data with the complex geometry of SWICS' entrance system and the trajectory data of Ulysses. For realizing this, a virtual detector, following the original geometry of SWICS, was built in Python. The detector's velocity acceptance was reconstructed in multiple steps. While the absolute velocity of He+ ions followed from the energy-per-charge information, three-dimensional components were obtained by SWICS' sector- and detector resolution. For the correct interpretation of these it was significant to consider the instrument's orientation. After having calculated this from data of Ulysses' and the Earth's orbit we were able to incorporate the spacecraft's aspect angle, SWICS' Orientation within the spacecraft's spin and Ulysses' eigen-velocity for every point in time.
After a consistency check with solar wind He2+ we were able to translate He+ Triple Coincidences into three-dimensional velocity components. A phase space normalization was necessary for translating counts into the physically relevant quantity phase space density. Finally, we presented three-dimensional velocity distributions using different projections.
These newly created three-dimensional data products can significantly contribute to a better understanding of PUI phase space transport. By the deconvolution of former 1D velocity spectra into directionally resolved spectra the evolution of the PUI VDFs can be studied in detail. Existing theory on processes that shape these distributions like cooling mechanisms and pitch-angle scattering can be tested directly. Ulysses' outstanding orbit that spans a wide range of solar radii particularly suggest exploring the radial evolution of these processes.
In future, the presented method could also be adapted to other PUI than He+, e.g. 06+ or He2+ – or even to solar wind ions.
In this work we could already confirm with our super duper method that He+ PUI feature sphere-like VDF.

.

In this work we decided for He+ PUI as a first approach for our method. Die hier vorgestellte Analyse wurde exemplarisch an He+ PUI durchgeführt und es konnten erstmalig von SWICS gemessene 3d VDF verteilungen präsentiert werden.

(vorher: nur Betrag. Jetzt: Komponenten).

Restrictions:
Auflösung eingeschränkt
Wir sind eingeschränkt auf schnellen SW
assumption: vsw nur radial
Efficiency müsste genau bestimmt werden: Dabei berücksichtigen, welcher Anteil unter den Threshold wandert. Evtl. überschätzen wir die Eff., wenn wir die interpolierten Werte von ACE/SWICS nehmen.

Appendix A

PSD – Sequence

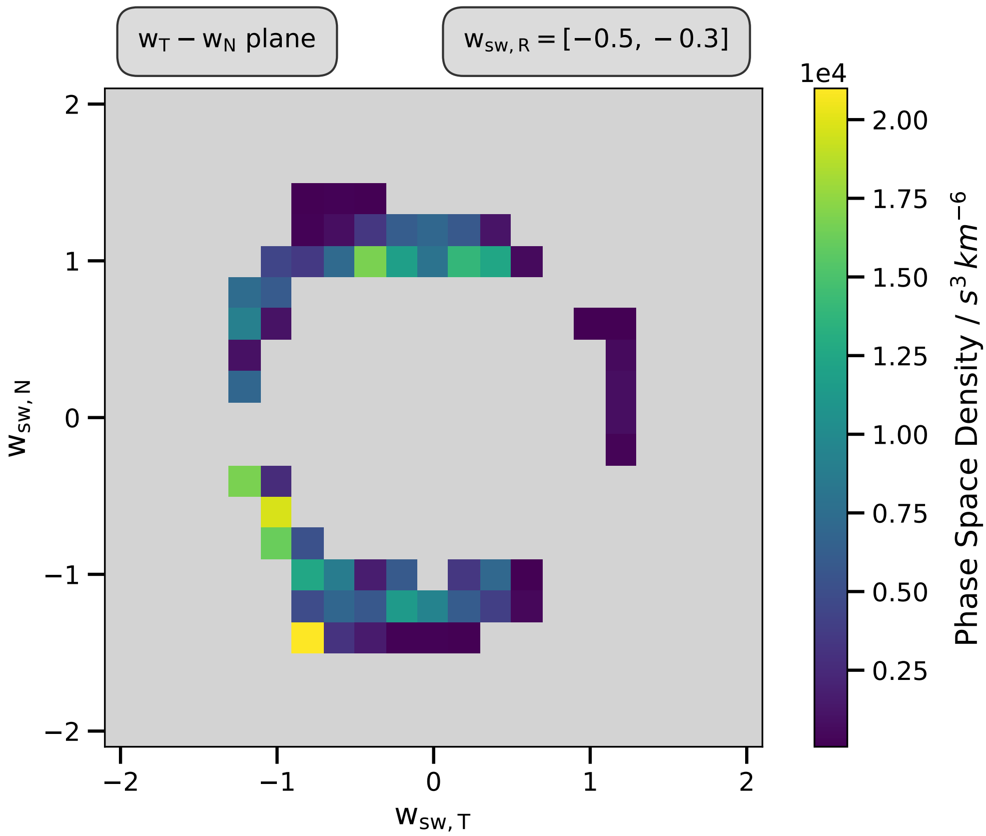

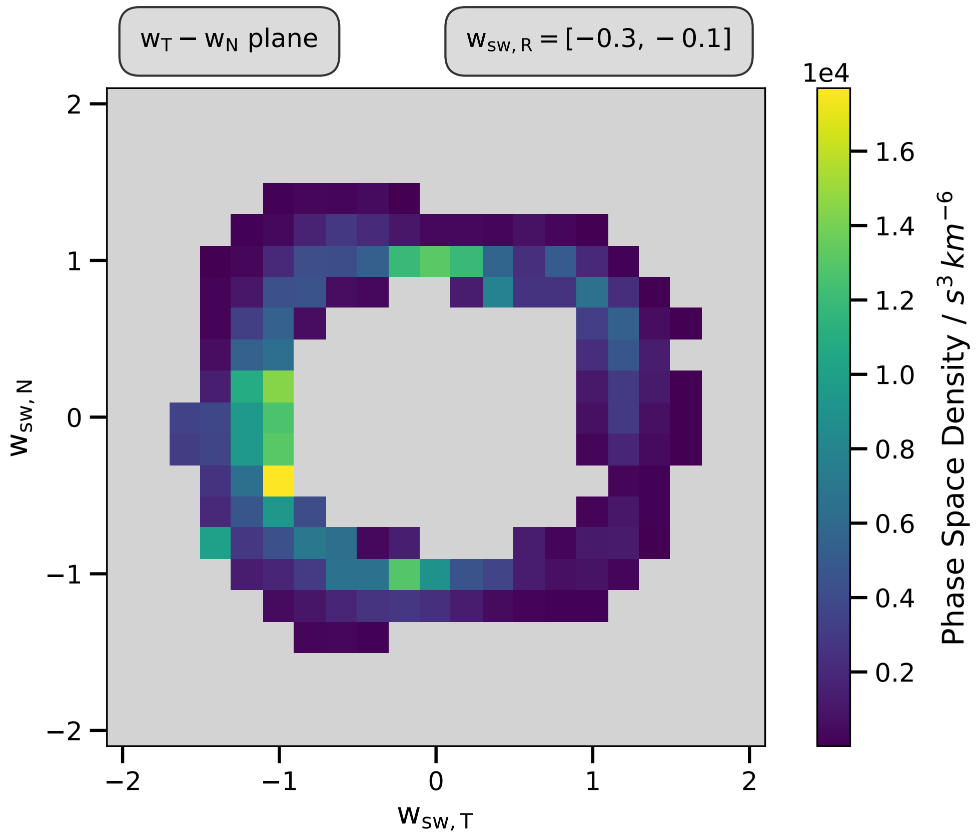

$w_T - w_N$ plane
$w_{sw,R} = [-0.3, -0.1]$
1e4
Phase Space Density / $s^3\,km^{-6}$
$w_{sw,N}$
$w_{sw,T}$

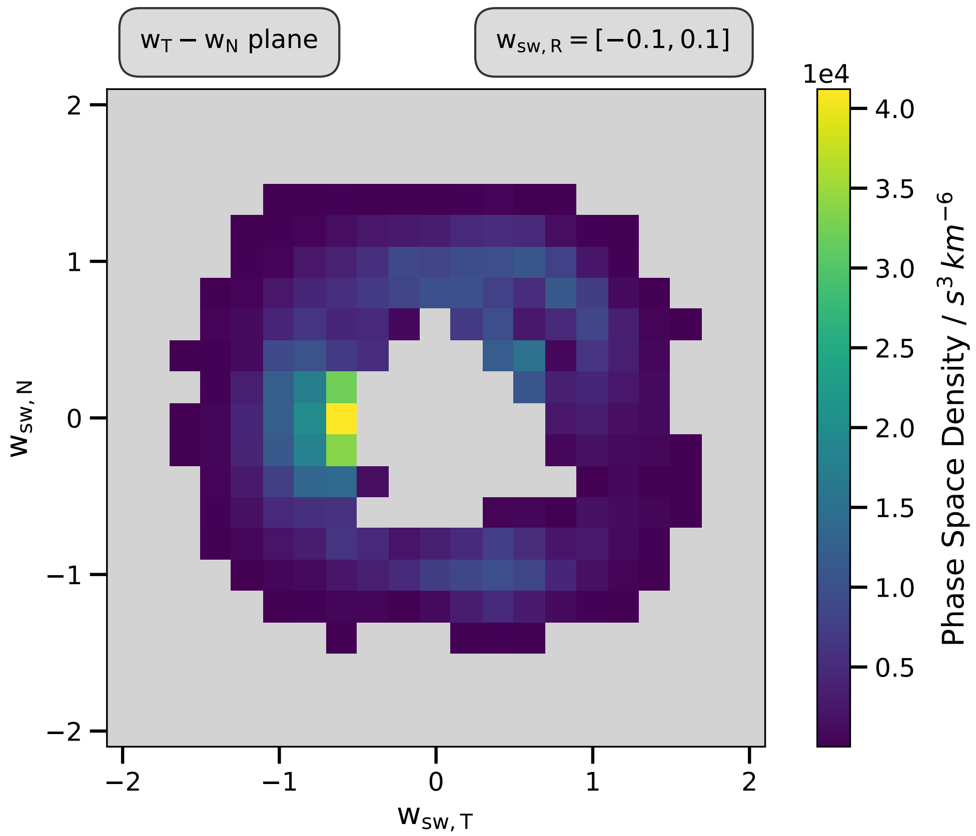

$w_T - w_N$ plane
$w_{sw,R} = [-0.1, 0.1]$
1e4
Phase Space Density / $s^3\,km^{-6}$
$w_{sw,N}$
$w_{sw,T}$

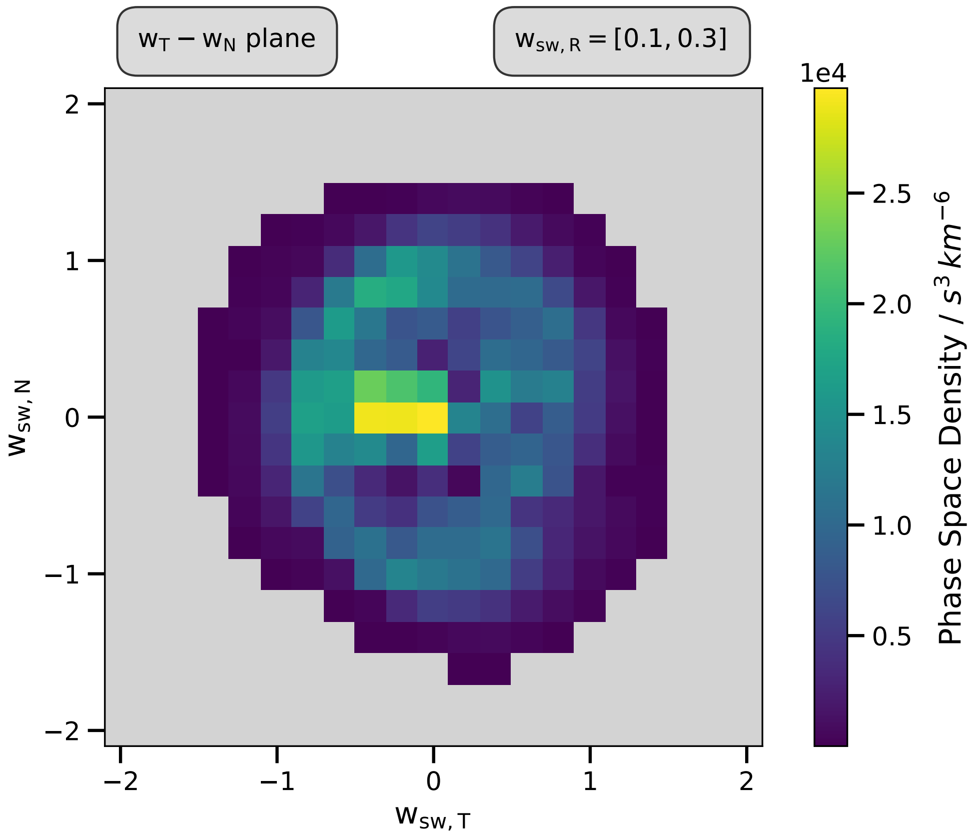
$w_T - w_N$ plane
$w_{sw,R} = [0.1, 0.3]$
1e4
2.5
2.0
1.5
1.0
0.5
Phase Space Density / $s^3\,km^{-6}$
$w_{sw,N}$
$w_{sw,T}$
2
1
0
−1
−2

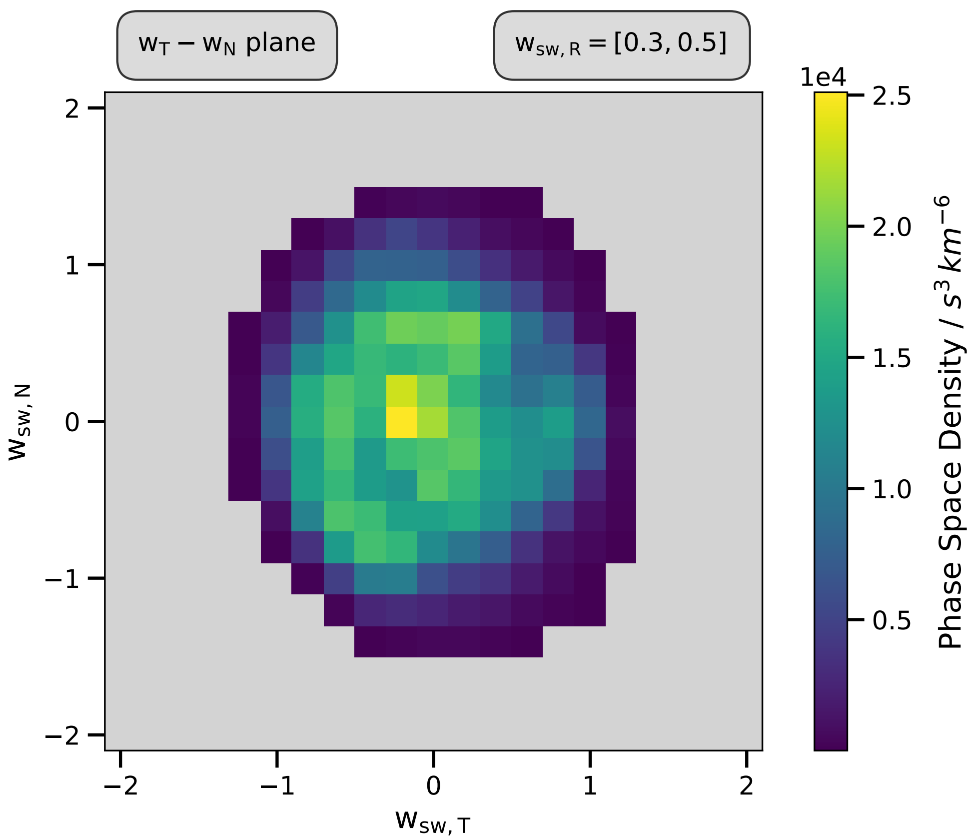
$w_T - w_N$ plane
$w_{sw,R} = [0.3, 0.5]$
1e4
2.5
2.0
1.5
1.0
0.5
Phase Space Density / $s^3\,km^{-6}$
$w_{sw,N}$
$w_{sw,T}$
2
1
0
−1
−2

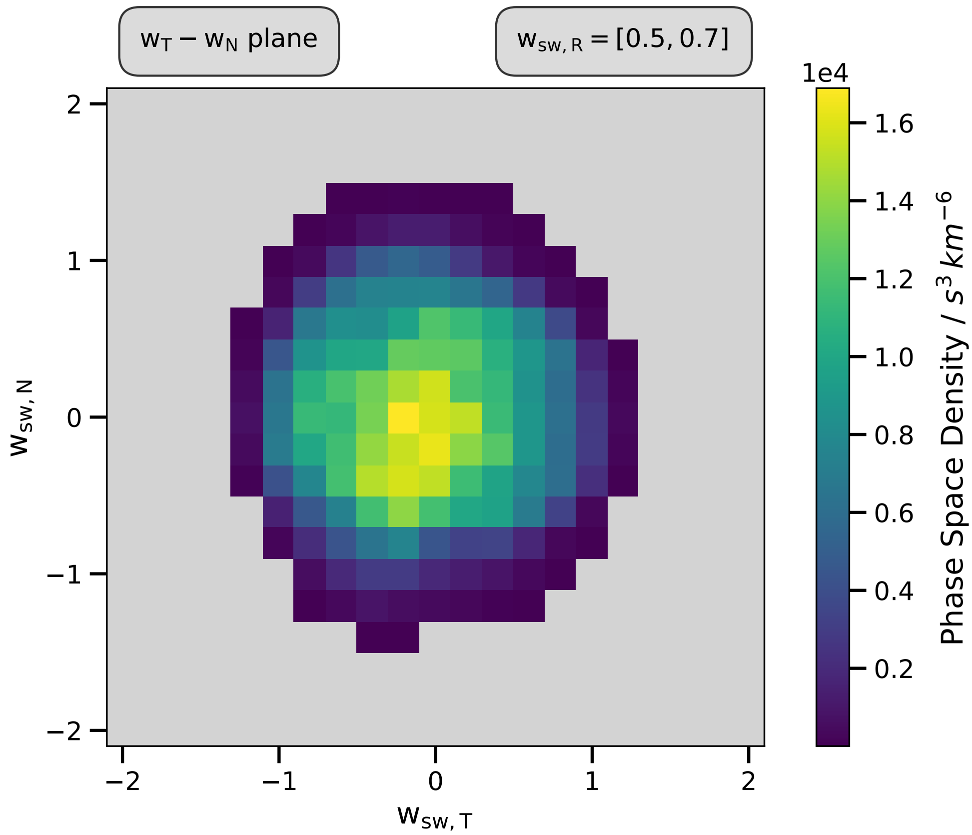

$w_T - w_N$ plane
$w_{sw,R} = [0.5, 0.7]$
$w_{sw,N}$
$w_{sw,T}$
1e4
Phase Space Density / $s^3\,km^{-6}$

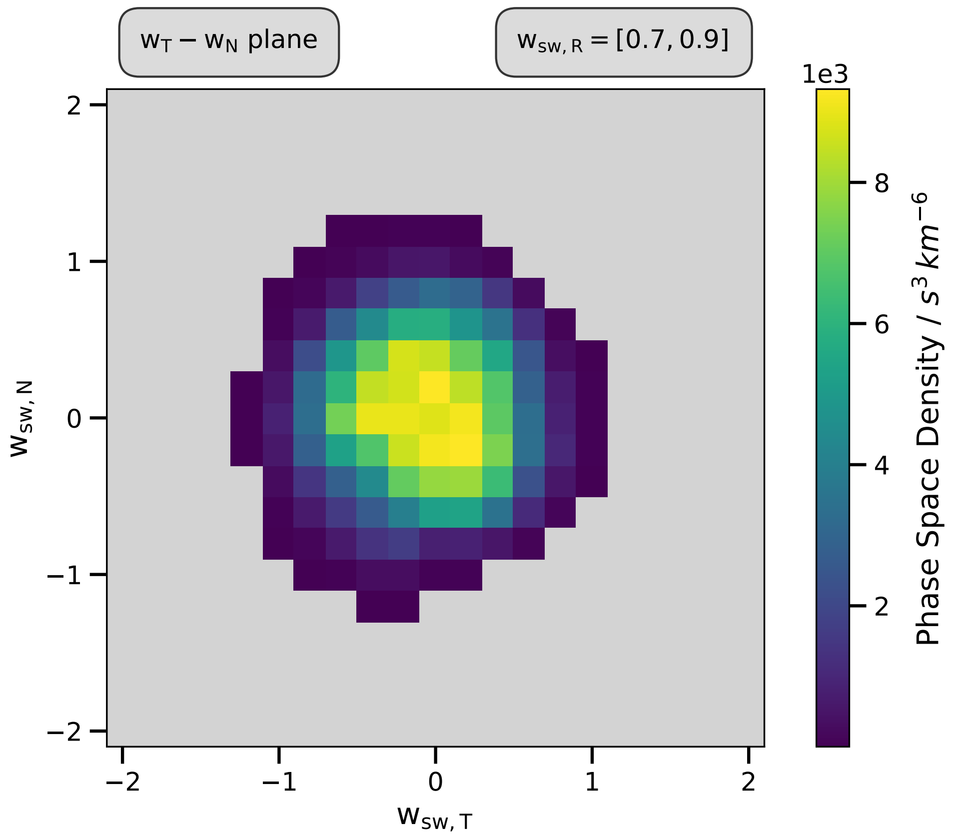

$w_T - w_N$ plane
$w_{sw,R} = [0.7, 0.9]$
$w_{sw,N}$
$w_{sw,T}$
1e3
Phase Space Density / $s^3\,km^{-6}$

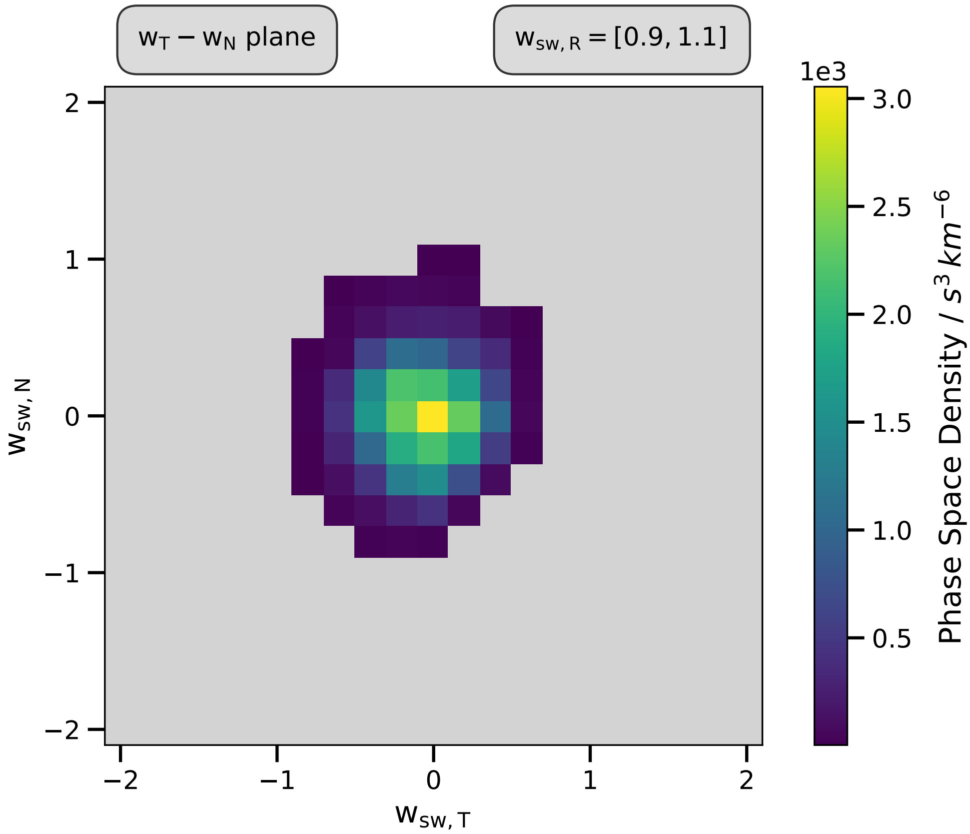

$w_T - w_N$ plane
$w_{sw,R} = [0.9, 1.1]$
1e3
3.0
2.5
2.0
1.5
1.0
0.5
Phase Space Density / $s^3\,km^{-6}$
$w_{sw,N}$
2
1
0
−1
−2
$w_{sw,T}$

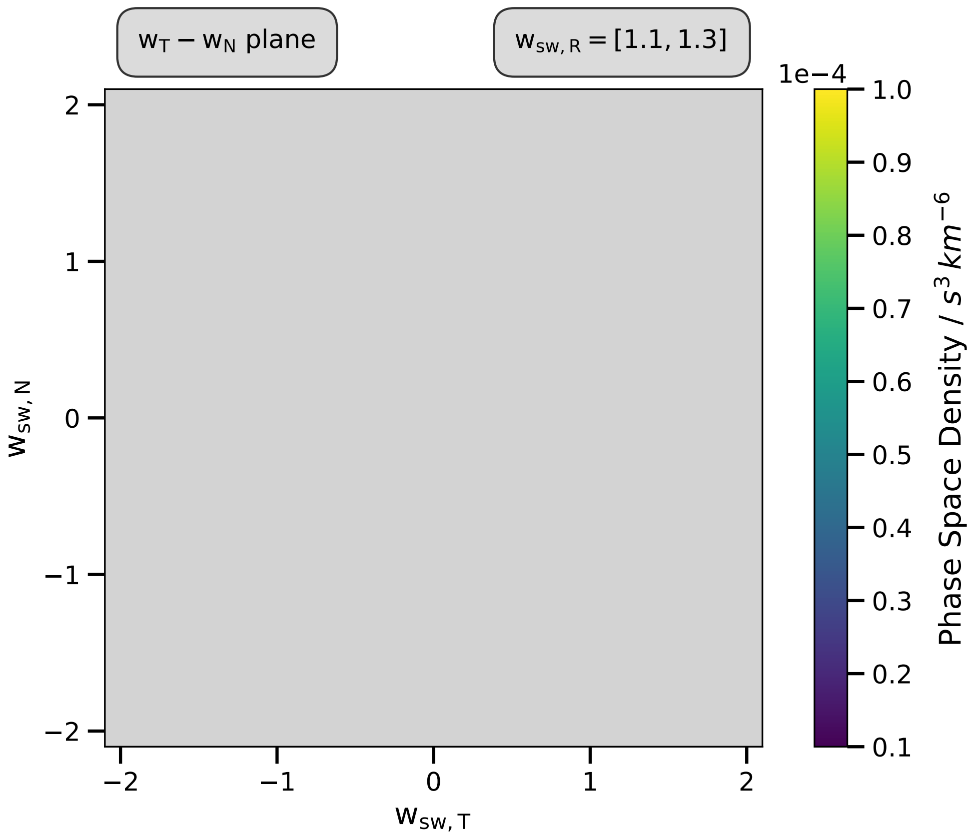

$w_T - w_N$ plane
$w_{sw,R} = [1.1, 1.3]$
1e−4
1.0
0.9
0.8
0.7
0.6
0.5
0.4
0.3
0.2
0.1
Phase Space Density / $s^3\,km^{-6}$
$w_{sw,N}$
2
1
0
−1
−2
$w_{sw,T}$

Bibliography

Allegrini, F., N. A. Schwadron, D. J. McComas, G. Gloeckler, and J. Geiss (May 2005). "Stability of the inner source pickup ions over the solar cycle". In: *Journal of Geophysical Research* 110.A5, A05105, A05105. DOI: 10.1029/2004JA010847.

Bame, S. J., D. J. McComas, B. L. Barraclough, J. L. Phillips, K. J. Sofaly, J. C. Chavez, B. E. Goldstein, and R. K. Sakurai (Jan. 1992). "The ULYSSES solar wind plasma experiment". In: *Astronomy and Astrophysics Supplement Series* 92.2, pp. 237–265.

Berger, Lars (2008). "Velocity Distribution Functions of Heavy Ions in the Solar Wind at 1 AU". PhD thesis. Christian-Albrechts-Universität zu Kiel, IEAP.

Drews, Christian, Lars Berger, Andreas Taut, Thies Peleikis, and Robert F. Wimmer-Schweingruber (Mar. 2015). "2D He^{+} pickup ion velocity distribution functions: STEREO PLASTIC observations". In: *Astronomy & Astrophysics* 575, A97, A97. DOI: 10.1051/0004-6361/201425271.

European Space Agency (2019). *ESA Website – Ulysses Orbit*. URL: https://www.cosmos.esa.int/web/ulysses/the-ulysses-orbit (visited on 10/27/2019).

Fahr, H. J. (Dec. 2007). "Revisiting the theory of the evolution of pick-up ion distributions: magnetic or adiabatic cooling?" In: *Annales Geophysicae* 25.12, pp. 2649–2659.

Fahr, H. J. and H. Fichtner (Sept. 2011). "Pickup ion transport under conservation of particle invariants: how important are velocity diffusion and cooling processes?" In: *Astronomy & Astrophysics* 533, A92, A92. DOI: 10.1051/0004-6361/201116880.

Fisk, L. A. and G. Gloeckler (Nov. 2012). "Particle Acceleration in the Heliosphere: Implications for Astrophysics". In: *Space Science Reviews* 173.1, pp. 433–458. ISSN: 1572-9672. DOI: 10.1007/s11214-012-9899-8. URL: https://doi.org/10.1007/s11214-012-9899-8.

Fränz, M. and D. Harper (Feb. 2002). "Heliospheric coordinate systems. Corrected Version". In: *Planetary & Space Science* 50.2, pp. 217–233. DOI: 10.1016/S0032-0633(01)00119-2.

Frisch, Priscilla C., Seth Redfield, and Jonathan D. Slavin (Sept. 2011). "The Interstellar Medium Surrounding the Sun". In: *Annual Review of Astronomy and Astrophysics* 49.1, pp. 237–279. DOI: 10.1146/annurev-astro-081710-102613.

Geiss, J., G. Gloeckler, L. A. Fisk, and R. von Steiger (1995). "C+ Pickup ions in the heliosphere and their origin". In: *Journal of Geophysical Research: Space Physics* 100.A12, pp. 23373–23377. DOI: 10.1029/95JA03051. eprint: https://agupubs.onlinelibrary.wiley.com/doi/pdf/10.1029/95JA03051. URL: https://agupubs.onlinelibrary.wiley.com/doi/abs/10.1029/95JA03051.

Geiss, J., G. Gloeckler, and R. von Steiger (Apr. 1995). "Origin of the solar wind from composition data". In: *Space Science Reviews* 72.1, pp. 49–60. ISSN: 1572-9672. DOI: 10.1007/BF00768753. URL: https://doi.org/10.1007/BF00768753.

Gloeckler, G. (July 1999). "Observation of Injection and Pre-Acceleration Processes in the Slow Solar Wind". In: *Space Science Reviews* 89, pp. 91–104. DOI: 10.1023/A:1005272601422.

Gloeckler, G., L. A. Fisk, J. Geiss, N. A. Schwadron, and T. H. Zurbuchen (Apr. 2000). "Elemental composition of the inner source pickup ions". In: *Journal of Geophysical Research* 105.A4, pp. 7459–7464. DOI: 10.1029/1999JA000224.

Gloeckler, G., J. Geiss, H. Balsiger, P. Bedini, J. C. Cain, J. Fischer, L. A. Fisk, A. B. Galvin, F. Gliem, D. C. Hamilton, J. V. Hollweg, F. M. Ipavich, R. Joos, S. Livi, R. A. Lundgren, U. Mall, J. F. McKenzie, K. W. Ogilvie, F. Ottens, W. Rieck, E. O. Tums, R. von Steiger, W. Weiss, and B. Wilken (Jan. 1992). "The Solar Wind Ion Composition Spectrometer". In: *Astronomy & Astrophysics Supplement Series* 92.2, pp. 267–289.

Gloeckler, G. and Johannes Geiss (July 1998). "Interstellar and Inner Source Pickup Ions Observed with SWICS on ULYSSES". In: *Space Science Reviews* 86, pp. 127–159. DOI: 10.1023/A:1005019628054.

Gloeckler, G., N. A. Schwadron, L. A. Fisk, and J. Geiss (Jan. 1995). "Weak pitch angle scattering of few MV rigidity ions from measurements of anisotropies in the distribution function of interstellar pickup H^+". In: *Geophysical Research Letters* 22.19, pp. 2665–2668. DOI: 10.1029/95GL02480.

Hunt-Ward, T. and T.P. Armstrong, eds. (1999). *Ulysses HISCALE Data Analysis Handbook*. Fundamental Technologies, LLC.

Isenberg, Philip A. (Mar. 1997). "A hemispherical model of anisotropic interstellar pickup ions". In: *Journal of Geophysical Research* 102.A3, pp. 4719–4724. DOI: 10.1029/96JA03671.

Kallenbach, R., J. Geiss, G. Gloeckler, and R. von Steiger (Oct. 2000). "Pick-up Ion Measurements in the Heliosphere – A Review". In: *Astrophysics and Space Science* 274.1, pp. 97–114. ISSN: 1572-946X. DOI: 10.1023/A:1026587620772. URL: https://doi.org/10.1023/A:1026587620772.

Kallenrode, May-Britt (1998). *Space Physics*. Springer.

Köten, Muharrem (Mar. 2009). "An improved efficiency model for ACE/SWICS - Determination of the carbon isotopic ratio 13 C/ 12 C in the solar wind from ACE/SWICS measurements". PhD thesis. Christian-Albrechts-Universität zu Kiel, IEAP.

McComas, D. J., N. A. Schwadron, F. J. Crary, H. A. Elliott, D. T. Young, J. T. Gosling, M. F. Thomsen, E. Sittler, J.-J. Berthelier, K. Szego, and A. J. Coates (2004). "The interstellar hydrogen shadow: Observations of interstellar pickup ions beyond Jupiter". In: *Journal of Geophysical Research: Space Physics* 109.A2. DOI: 10.1029/2003JA010217. eprint: https://agupubs.onlinelibrary.wiley.com/doi/pdf/10.1029/2003JA010217. URL: https://agupubs.onlinelibrary.wiley.com/doi/abs/10.1029/2003JA010217.

Möbius, E., D. Hovestadt, B. Klecker, G. Scholer, and G. Gloeckler (1985). "Direct observation of He+ pick-up ions of interstellar origin in the solar wind". In: *nature* 318 (6045), pp. 426–429. DOI: 10.1038/318426A0.

Möbius, E., D. Rucinski, M. A. Lee, and P. A. Isenberg (Jan. 1998). "Decreases in the antisunward flux of interstellar pickup He^+ associated with radial interplanetary magnetic field". In: *Journal of Geophysical Research* 103.A1, pp. 257–266. DOI: 10.1029/97JA02771.

NASA HelioWeb (2019). *Heliocentric Trajectories for Selected Spacecraft, Planets, and Comets*. URL: https://omniweb.gsfc.nasa.gov/coho/helios/heli.html (visited on 06/01/2019).

Oka, M., T. Terasawa, H. Noda, Y. Saito, and T. Mukai (June 2002). "'Torus' distribution of interstellar helium pickup ions: Direct observation". In: *Geophysical Research Letters* 29.12, 1612, p. 1612. DOI: 10.1029/2002GL015111.

Prölss, Gerd W. (2004). *Physik des erdnahen Weltraums. Eine Einführung*. Springer Berlin Heidelberg. DOI: 10.1007/978-3-642-18807-7.

Rucinski, D., A. C. Cummings, G. Gloeckler, A. J. Lazarus, E. Möbius, M., and Witte (Oct. 1996). "Ionization processes in the heliosphere – Rates and methods of their determination". In: *Space Science Reviews* 78.1-2, pp. 73–84. DOI: 10.1007/BF00170794.

Schwadron, N. A., J. Geiss, L. A. Fisk, G. Gloeckler, T. H. Zurbuchen, and R. von Steiger (Apr. 2000). "Inner source distributions: Theoretical interpretation, implications, and evidence for inner source protons". In: *Journal of Geophysical Research* 105.A4, pp. 7465–7472. DOI: 10.1029/1999JA000225.

Schwadron, N. A., E. Möbius, T. Leonard, S. A. Fuselier, D. J. McComas, D. Heirtzler, H. Kucharek, F. Rahmanifard, M. Bzowski, M. A. Kubiak, J. M. Sokół, P. Swaczyna, and P. Frisch (Oct. 2015). "Determination of Interstellar He Parameters Using Five Years of Data from the IBEX: Beyond Closed Form Approximations". In: *The Astrophysical Journal Supplement Series* 220.2, 25, p. 25. DOI: 10.1088/0067-0049/220/2/25.

Stone, E. C., A. M. Frandsen, R. A. Mewaldt, E. R. Christian, D. Margolies, J. F. Ormes, and F. Snow (July 1998). "The Advanced Composition Explorer". In: *Space Science Reviews* 86, pp. 1–22. DOI: 10.1023/A:1005082526237.

SWICS DPU (1988). Ed. by F. Gliem, W. Rieck, and H. Dinse.

Taut, Andreas, Lars Berger, Christian Drews, Duncan Keilbach, Eberhard Möbius, and Martin A. Lee (2017). *Presentation: Pickup Ion Transport Effects? Challenges in the Determination of the Interstellar Flow Longitude Using the Pickup Ion Cutoff*.

Ulysses Final Archive (2008). Ed. by European Space Agency. URL: http://ufa.esac.esa.int/ufa/#data (visited on 08/01/2019).

Vasyliunas, V. M. and G. L. Siscoe (1976). "On the flux and the energy spectrum of interstellar ions in the solar system". In: *Journal of Geophysical Research (1896-1977)* (7).

Wenzel, K. P., R. G. Marsden, D. E. Page, and E. J. Smith (Jan. 1992). "The ULYSSES Mission". In: *Astronomy and Astrophysics Supplement* 92, p. 207.

Wimmer-Schweingruber, R. F. and P. Bochsler (May 2002). "On the Origin of Inner-Source Pickup Ions". In: *Geophysical Research Letters* 30.2, pp. 49-1 - 49–4.

Eidesstattliche Erklärung

Hiermit erkläre ich, dass ich die vorliegende Masterarbeit selbständig und lediglich unter Benutzung der angegebenen Quellen und Hilfsmittel verfasst habe. Ferner versichere ich, dass die vorliegende Arbeit noch nicht im Rahmen eines anderen Prüfungsverfahrens eingereicht wurde.

Ort, Datum:

Unterschrift:

Danksagung

The acknowledgments and the people to thank go here, don’t forget to include your project advisor…